submitted to *Geophys. J. Int.*

Advanced three-dimensional electromagnetic modeling using a nested integral equation approach

Chaojian Chen[1], Mikhail Kruglyakov[1,2] and Alexey Kuvshinov[1]

[1] *Institute of Geophysics, ETH Zürich, Zürich, Switzerland. Email: chaojian.chen@erdw.ethz.ch*

[2] *Geoelectromagnetic Research Center, Institute of Physics of the Earth, Moscow, Russia.*

21 November 2020

SUMMARY

Most of the existing three-dimensional (3-D) electromagnetic (EM) modeling solvers based on the integral equation (IE) method exploit fast Fourier transform (FFT) to accelerate the matrix-vector multiplications. This in turn requires a laterally-uniform discretization of the modeling domain. However, there is often a need for multi-scale modeling and inversion, for instance, to properly account for the effects of non-uniform distant structures, and at the same time, to accurately model the effects from local anomalies. In such scenarios, the usage of laterally-uniform grids leads to excessive computational loads, both in terms of memory and time. To alleviate this problem, we developed an efficient 3-D EM modeling tool based on a multi-nested IE approach. Within this approach the IE modeling is first performed at a large domain and on a (laterally-uniform) coarse grid, and then the results are refined in the region of interest by performing modeling at a smaller domain and on a (laterally-uniform) denser grid. At the latter stage, the modeling results obtained at the previous stage are exploited. The lateral uniformity of the grids at each stage allows us to keep using the FFT, and thus attain the remarkable performance of the developed tool. An important novelty of the paper is a development of a "rim domain" concept which further improves the efficiency of the multi-nested IE approach.

Key words: Electromagnetic theory; Geomagnetic induction; Magnetotellurics; Numerical modelling.

1 INTRODUCTION

Electromagnetic (EM) methods in geophysics aim to constrain the electrical conductivity of the Earth's interior. Since the conductivity is sensitive to the temperature, chemical composition and water content, it helps to understand the Earth's origin, past evolution and modern dynamics (Yoshino 2010; Chave & Jones 2012; Karato & Wang 2013; Khan 2016; Johansen et al. 2019). Nowadays, an immense amount of EM data is available at different scales – from global to local – including the data from a global network of geomagnetic observatories (St-Louis et al. 2011), low-orbit satellites (Olsen & Floberghagen 2018), continental-scale magnetotelluric (MT) surveys (Chopping et al. 2016; Dong & Li 2010; Schultz 2010), as well as from numerous regional and local EM field campaigns around the world. Most of the modern data sets require an interpretation in terms of three-dimensional (3-D) conductivity models. To perform credible and comprehensive interpretation, robust and efficient 3-D EM modeling tools are of vital importance.

There are four basic numerical simulation techniques for computing the frequency-domain EM fields and responses in the 3-D Earth's conductivity models, namely finite difference (FD) (Mackie et al. 1994; Newman & Alumbaugh 2002; Egbert & Kelbert 2012; Dong & Egbert 2019; Li et al. 2019b), finite element (FE) (Key & Weiss 2006; Farquharson & Miensopust 2011; Ren et al. 2013a; Grayver & Kolev 2015; Li et al. 2019a), finite volume (FV) (Haber & Ascher 2001; Haber & Ruthotto 2014; Jahandari & Farquharson 2014; Han et al. 2018), and integral equation (IE) (Avdeev et al. 2002a; Hursan & Zhdanov 2002; Koyama et al. 2008; Singer 2008) methods. The solvers based on FD, FE, and FV methods have the advantage that they generate a sparse system of linear equations, and non-uniform grids can be adopted to approximate complicated structures, for instance, topography and bathymetry. However, these solvers require a discretization of the volume which is much larger than the volume occupied by the 3-D anomalies under consideration, and, moreover,

the generated system of linear equations is usually poorly conditioned, thus requiring preconditioning. In contrast, the solvers based on the IE method only need a discretization of 3-D anomalies, which eventually leads to a smaller (but dense) matrix. Moreover, combined with the contraction operator (Pankratov & Kuvshinov 2016), the IE technique generates a well-conditioned system of linear equations, which can be effectively solved by using iterative methods. In this paper, we report our progress in further advancing the numerical tools based on the IE method, confining, however, ourselves to the flat Earth (Cartesian geometry) problem setups.

As mentioned before, the drawback of IE method is that it generates a dense matrix, which leads to a large computational complexity. This means that the IE method requires prohibitive computational loads if dealing with large-scale (in terms of the number of unknowns) problems. In the past several decades, significant efforts have been undertaken to improve the performance of the IE method. For instance, the matrix decomposition (MD) algorithm (Canning 1989; Sun & Kuvshinov 2015), fast multipole method (FMM) (Gumerov & Duraiswami 2005; Ren et al. 2013b) and fast Fourier transform (FFT) (Avdeev et al. 2002a; Hursan & Zhdanov 2002; Singer 2008; Kruglyakov & Bloshanskaya 2017, among others) were invoked to accelerate the matrix-vector multiplication – one of the core operations in the IE method – as well as to reduce the memory requirement. The MD method is rather straightforward, but in general is slower than FMM and FFT algorithms. FMM is relatively fast but intricate in implementation. In this paper we exploit the FFT approach as a baseline for the improved performance of the IE method.

When Cartesian geometry is invoked in the IE method, the usage of the two-dimensional (2-D) fast Fourier transform algorithm in lateral directions tremendously reduces the computational loads in terms of both memory and CPU time, but requires a laterally-uniform grid. However, rather often the researchers encounter situations when the data interpretation necessitates multi-scale modeling and inversion, for instance, to appropriately take into account the effects from inhomogeneous remote structures, and at the same time to accurately model the effects from local inhomogeneities, like topography and bathymetry. In this

case, the usage of laterally-uniform grids leads to prohibitively high computational loads even when the 2-D FFT is used. To alleviate this problem Nie et al. (2013) and Kamm & Pedersen (2014) applied the pre-corrected FFT method to use the non-uniform grid in the modeling domain. In their approach, the nested FFTs are utilized to approximate matrix-vector multiplication when iteratively solving the system of linear equations (Phillips & White 1997). Another approach to address the problem is to work with nested, but still uniformly discretized, *domains*. Specifically, modeling is first performed at a large domain and on a coarse grid, and then the results are refined by performing modeling at a smaller domain and on a finer grid, exploiting at the latter step the previous "coarser grid" results.

This nested domains approach was discussed in a two-step realization by Avdeev et al. (2002) and Kuvshinov et al. (2005) as applied to the induction logging and global EM induction problems, respectively, but both studies presented prototype solutions rather than usable tools. Recently we developed a two-step nested IE-based tool (Chen et al. 2020) which combines the global IE (Kuvshinov 2008) and Cartesian IE (Kruglyakov & Kuvshinov 2018) solvers, and allows researchers to efficiently and accurately model the ocean induction effect in the long-period EM responses. Note that the global solver works in spherical geometry and thus – in contrast to the Cartesian case – allows the application of the FFT in one lateral direction only. Inspired by the successful implementation of the two-step nested IE approach in mixed (spherical and Cartesian) geometries, in this paper we present a nested IE-based modeling tool that exclusively works in the flat (Cartesian) Earth's models. In contrast to aforementioned (two-step) solutions, our tool may include multiple steps thus allowing recursively an increase in detail of the model in the region of interest. Moreover we introduce in the paper a new, "rim domain" concept, which further improves the efficacy of the nested IE approach.

The structure of the paper is as follows. Section 2 presents the theoretical aspects of IE in both conventional and nested versions. Section 3 provides the implementation details of a nested IE approach. Section 4 discusses the verification of the developed tool on an example of two 3-D conductivity models. Section 5 summarizes the results of the paper and discusses

the potential directions of the future work. The paper also contains two appendices which further detail the numerical implementation of the nested approach.

2 THEORY

2.1 Conventional IE method

The frequency-domain electric and magnetic fields, $\mathbf{E}$ and $\mathbf{H}$, induced by the impressed (extraneous) current, $\mathbf{j}^{\rm imp}$, obey Maxwell's equations

$$\nabla \times \mathbf{H} = \sigma \mathbf{E} + \mathbf{j}^{\rm imp}, \tag{1}$$

$$\nabla \times \mathbf{E} = i\omega\mu_0 \mathbf{H}. \tag{2}$$

Here $\sigma(\mathbf{r})$ stands for a three-dimensional conductivity distribution in a model Earth, $\mathbf{r} = (x, y, z)$ denotes a right-handed Cartesian coordinate system, $i = \sqrt{-1}$, μ_0 is the magnetic permeability of free space, and ω is the angular frequency. Time dependence is accounted for by $e^{-i\omega t}$. This formulation neglects the displacement currents, which are irrelevant in the frequency range of our interest (10^{-4} – 10^{4} Hz).

An IE approach requires introducing a one-dimensional (1-D; background) conductivity distribution $\sigma_0(z)$, and the background electric and magnetic fields, $\mathbf{E}^0$ and $\mathbf{H}^0$, which are the solutions of Maxwell's equations

$$\nabla \times \mathbf{H}^0 = \sigma_0 \mathbf{E}^0 + \mathbf{j}^{\rm imp}, \tag{3}$$

$$\nabla \times \mathbf{E}^0 = i\omega\mu_0 \mathbf{H}^0. \tag{4}$$

The fields $\mathbf{E}^0$ and $\mathbf{H}^0$ can be obtained at any location as

$$\mathbf{E}^0(\mathbf{r}) = \int\limits_{\rm V^{imp}} \widehat{G}^{ej}(\mathbf{r}, \mathbf{r}') \mathbf{j}^{\rm imp}(\mathbf{r}') d{\rm V}, \quad \mathbf{r} \in \mathbf{R}^3, \tag{5}$$

$$\mathbf{H}^0(\mathbf{r}) = \int\limits_{\rm V^{imp}} \widehat{G}^{hj}(\mathbf{r}, \mathbf{r}') \mathbf{j}^{\rm imp}(\mathbf{r}') d{\rm V}, \quad \mathbf{r} \in \mathbf{R}^3, \tag{6}$$

where, $\rm V^{imp}$ is the volume occupied by $\mathbf{j}^{\rm imp}$, and $\widehat{G}^{ej}$, $\widehat{G}^{hj}$ are the current-to-electric and current-to-magnetic Green's tensors, respectively (cf. Avdeev et al. 2002a; Kruglyakov &

Bloshanskaya 2017). Note that the fields and the current depend on ω, and Green's tensors depend on ω and $\sigma_0(z)$, however, hereafter we will omit but imply these dependencies.

By knowing $\widehat{G}^{ej}$ and $\widehat{G}^{hj}$, the electric and magnetic field solutions of eqs (1)-(2) can be written as

$$\mathbf{E}(\mathbf{r}) = \mathbf{E}^0(\mathbf{r}) + \int_{\mathrm{V}} \widehat{G}^{ej}(\mathbf{r},\mathbf{r}')\Delta\sigma(\mathbf{r}')\mathbf{E}(\mathbf{r}')d\mathrm{V}, \quad \mathbf{r} \in \mathbf{R}^3, \tag{7}$$

$$\mathbf{H}(\mathbf{r}) = \mathbf{H}^0(\mathbf{r}) + \int_{\mathrm{V}} \widehat{G}^{hj}(\mathbf{r},\mathbf{r}')\Delta\sigma(\mathbf{r}')\mathbf{E}(\mathbf{r}')d\mathrm{V}, \quad \mathbf{r} \in \mathbf{R}^3, \tag{8}$$

where V is the region where $\Delta\sigma = \sigma - \sigma_0 \neq 0$. If one finds $\mathbf{E}$ in V, one can then compute $\mathbf{E}$ and $\mathbf{H}$ at any location in space using appropriate Green's tensors. In order not to overload the narration, from now on we will discuss the computation of $\mathbf{E}$ only; $\mathbf{H}$ is computed in a similar way.

To find $\mathbf{E}(\mathbf{r})$ in V one has to numerically solve the integral equation

$$\mathbf{E}(\mathbf{r}) - \int_{\mathrm{V}} \widehat{G}^{ej}(\mathbf{r},\mathbf{r}')\Delta\sigma(\mathbf{r}')\mathbf{E}(\mathbf{r}')d\mathrm{V} = \mathbf{E}^0(\mathbf{r}), \quad \mathbf{r} \in \mathrm{V}. \tag{9}$$

As mentioned in the introduction, after discretization of the above equation the resulting system matrix is dense. Hence, in the general case, the computational load (time and memory) to compute the system matrix and to solve the corresponding system with N unknowns is $\mathcal{O}(N^2)$, meaning that with realistic (large) N the problem becomes computationally demanding.

The conventional way to deal with this challenge is to exploit the fact that $\widehat{G}^{ej}$ has convolution properties in lateral directions (Avdeev et al. 1997; Kruglyakov & Bloshanskaya 2017)

$$\widehat{G}^{ej}(\mathbf{r},\mathbf{r}') = \widehat{G}^{ej}(x-x', y-y', z, z'). \tag{10}$$

Making use of the above convolution property and employing laterally-uniform discretization, the system matrix becomes block-Toeplitz which allows us to decrease memory requirements down to $\mathcal{O}(N_\tau)$ (cf. Kruglyakov & Bloshanskaya 2017), where N_τ is the number of unknowns in lateral directions. Moreover, the usage of 2-D FFT for performing matrix-vector multiplications – which are needed to (iteratively) solve the resulting system of linear equa-

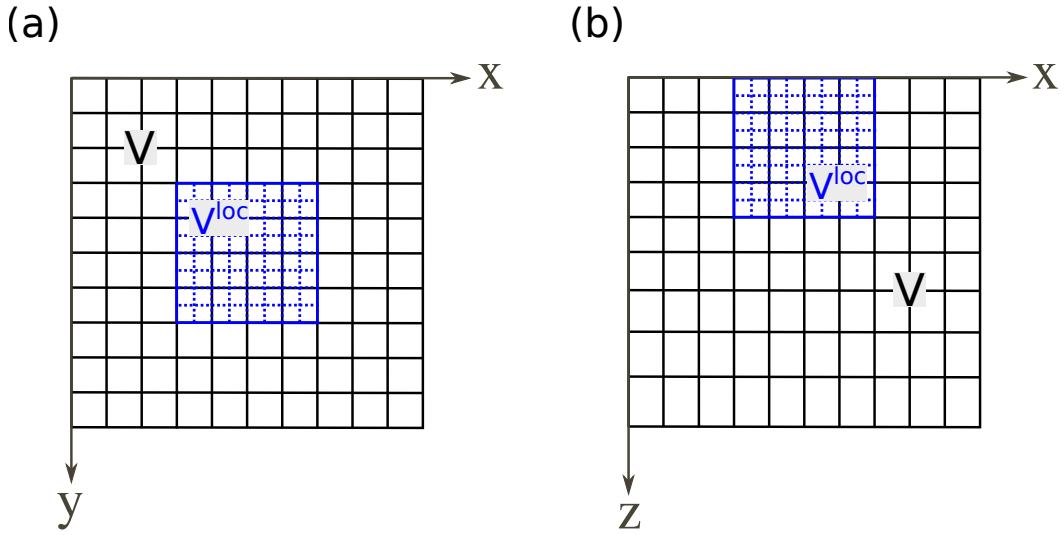

Figure 1. Illustration of the nested IE approach on an example of two-step realization: (a) a top view and (b) the cross section. The whole modeling domain V is divided into two parts: the local domain $\mathrm{V}^{\mathrm{loc}}$ and it's complement $\mathrm{V}^{\mathrm{out}}$.

tions – leads to computational time reduction with respect to N_τ unknowns to $\mathcal{O}(N_\tau \ln N_\tau)$. However, using laterally uniform discretization might still require large computational resources, when, for example, the problem setup dictates a large size of V and fine spatial resolution locally. In the next section, we present an approach to efficiently tackle such problem setups.

2.2 Nested IE (NIE) approach

Let us split the modeling domain V onto $\mathrm{V}^{\mathrm{loc}}$ and $\mathrm{V}^{\mathrm{out}}$ (see Figure 1), where $\mathrm{V}^{\mathrm{out}}$ is the complement of $\mathrm{V}^{\mathrm{loc}}$ to V, i.e.

$$\mathrm{V}^{\mathrm{out}} = \mathrm{V} \setminus \mathrm{V}^{\mathrm{loc}}. \tag{11}$$

Then, for $\mathbf{r} \in \mathrm{V}^{\mathrm{loc}}$, we can rewrite eq. (9) as

$$\mathbf{E}(\mathbf{r}) - \int\limits_{\mathrm{V}^{\mathrm{loc}}} \widehat{G}^{ej}(\mathbf{r},\mathbf{r}')\Delta\sigma(\mathbf{r}')\mathbf{E}(\mathbf{r}')d\mathrm{V} = \mathbf{E}^0(\mathbf{r}) + \mathbf{E}^{add}(\mathbf{r}), \quad \mathbf{r} \in \mathrm{V}^{\mathrm{loc}}, \tag{12}$$

where

$$\mathbf{E}^{add}(\mathbf{r}) = \int\limits_{\mathrm{V}^{\mathrm{out}}} \widehat{G}^{ej}(\mathbf{r},\mathbf{r}')\Delta\sigma(\mathbf{r}')\mathbf{E}(\mathbf{r}')d\mathrm{V}, \quad \mathbf{r} \in \mathrm{V}^{\mathrm{loc}}. \tag{13}$$

The key idea of the nested IE approach (cf. Avdeev et al. 2002; Kuvshinov et al. 2005; Chen et al. 2020) is to first solve the conventional IE at a coarse grid in the whole domain V

$$\mathbf{E}^{(c)}(\mathbf{r}) - \int\limits_{\mathrm{V}} \widehat{G}^{ej}(\mathbf{r},\mathbf{r}')\Delta\sigma^{(c)}(\mathbf{r}')\mathbf{E}^{(c)}(\mathbf{r}')d\mathrm{V} = \mathbf{E}^{0}(\mathbf{r}), \quad \mathbf{r}\in\mathrm{V}, \tag{14}$$

then calculate $\mathbf{E}^{add}(\mathbf{r})$ at a finer grid in $\mathrm{V}^{\mathrm{loc}}$ using $\mathbf{E}^{(c)}(\mathbf{r})$ calculated at a coarse grid in $\mathrm{V}^{\mathrm{out}}$

$$\mathbf{E}^{add\,(c)}(\mathbf{r}) = \int\limits_{\mathrm{V}^{\mathrm{out}}} \widehat{G}^{ej}(\mathbf{r},\mathbf{r}')\Delta\sigma^{(c)}(\mathbf{r}')\mathbf{E}^{(c)}(\mathbf{r}')d\mathrm{V}, \quad \mathbf{r}\in\mathrm{V}^{\mathrm{loc}}, \tag{15}$$

and eventually solve IE at a finer grid in $\mathrm{V}^{\mathrm{loc}}$

$$\mathbf{E}^{(f)}(\mathbf{r}) - \int\limits_{\mathrm{V}^{\mathrm{loc}}} \widehat{G}^{ej}(\mathbf{r},\mathbf{r}')\Delta\sigma^{(f)}(\mathbf{r}')\mathbf{E}^{(f)}(\mathbf{r}')d\mathrm{V} = \mathbf{E}^{0}(\mathbf{r}) + \mathbf{E}^{add\,(c)}(\mathbf{r}), \quad \mathbf{r}\in\mathrm{V}^{\mathrm{loc}}. \tag{16}$$

Here superscripts $^{(c)}$ and $^{(f)}$ mean that coarse and fine spatial resolutions are applied to obtain the corresponding quantities.

Once eq. (16) is solved, the electric field, $\mathbf{E}$, can be calculated at any point as

$$\mathbf{E}(\mathbf{r}) = \mathbf{E}^{0}(\mathbf{r}) + \int\limits_{\mathrm{V}^{\mathrm{loc}}} \widehat{G}^{ej}(\mathbf{r},\mathbf{r}')\Delta\sigma^{(f)}(\mathbf{r}')\mathbf{E}^{(f)}(\mathbf{r}')d\mathrm{V} + \mathbf{E}^{add\,(c)}(\mathbf{r}), \quad \mathbf{r}\in\mathbf{R}^{3}, \tag{17}$$

where

$$\mathbf{E}^{add\,(c)}(\mathbf{r}) = \int\limits_{\mathrm{V}^{\mathrm{out}}} \widehat{G}^{ej}(\mathbf{r},\mathbf{r}')\Delta\sigma^{(c)}(\mathbf{r}')\mathbf{E}^{(c)}(\mathbf{r}')d\mathrm{V}, \quad \mathbf{r}\in\mathbf{R}^{3}. \tag{18}$$

Note that the nested approach is discussed above in a two-step version for the sake of simplicity; one can, however, apply it recursively by exploiting a sequence of local domains $\mathrm{V}_1^{\mathrm{loc}} \subset \mathrm{V}_2^{\mathrm{loc}} \subset \ldots \mathrm{V}$. Later in the paper we will present the results of multi-step realization of the approach.

As evident, the nested approach requires solving IE numerically which is done by means of the Galerkin method. An outline of the method as applied to our problem is presented in the next section; the detailed description can be found in Kruglyakov & Bloshanskaya (2017) and Kruglyakov & Kuvshinov (2018).

149 ### 2.3 Galerkin method in a nutshell

Let $\mathcal{L}_2[\mathrm{V}]$ be a vector Hilbert functional space equipped with the dot product

$$(\mathbf{W},\mathbf{U}) = \int\limits_{\mathrm{V}} \left(W_x(\mathbf{r})\overline{U}_x(\mathbf{r}) + W_y(\mathbf{r})\overline{U}_y(\mathbf{r}) + W_z(\mathbf{r})\overline{U}_z(\mathbf{r})\right) d\mathrm{V}, \tag{19}$$

where $\overline{U}$ denotes the complex conjugation of U. Let the set of vector real-valued functions $\mathbf{\Psi}_n$, $n = 1, 2, \ldots, N$ form the orthonormal basis in $\mathcal{L}_2[\mathrm{V}]$. We then denote the linear span of this basis as Q^N and define the projection operator $\mathrm{P_N}$ from $\mathcal{L}_2[\mathrm{V}]$ to Q^N as

$$\mathbf{W}^N = \mathrm{P_N}\,\mathbf{W} = \sum_{n=1}^{N} a_n \mathbf{\Psi}_n, \quad \mathbf{W} \in \mathcal{L}_2[\mathrm{V}], \quad \mathbf{W}^N \in Q^N, \tag{20}$$

where

$$a_n = (\mathbf{W}, \mathbf{\Psi}_n). \tag{21}$$

The Galerkin method as applied to eq. (9) is based on an approximation of the function $\mathbf{E}$ inside V by the function $\mathbf{U} \in Q^N$ which satisfies the equations

$$((\mathrm{I} - \mathrm{G_E}\,\Delta\sigma)\,\mathbf{U}, \mathbf{\Psi}_n) = (\mathbf{E}^0, \mathbf{\Psi}_n), \quad n = 1, 2, \ldots, N, \tag{22}$$

where I is the identity operator, and $\mathrm{G_E}$ is the integral operator from eq. (9). Using the expansion

$$\mathbf{U} = \sum_{n=1}^{N} u_n \mathbf{\Psi}_n, \tag{23}$$

eq. (22) is transformed into the system of linear equations for coefficients u_n

$$u_n - \sum_{m=1}^{N} u_m (\mathrm{G_E}\,\Delta\sigma\mathbf{\Psi}_m, \mathbf{\Psi}_n) = (\mathbf{E}^0, \mathbf{\Psi}_n), \quad n = 1, 2, \ldots, N. \tag{24}$$

After solving the system (24) (see Kruglyakov & Bloshanskaya (2017) and Kruglyakov & Kuvshinov (2018) for details of efficient numerical implementation) one substitutes $\mathbf{U}$ instead of $\mathbf{E}$ into the integrands in eq. (7) to obtain the (approximation of) electric field, $\widetilde{\mathbf{E}}$, at any point as

$$\widetilde{\mathbf{E}}(\mathbf{r}) = \mathbf{E}^0(\mathbf{r}) + \sum_{n=1}^{N} u_n \int\limits_{\mathrm{V}} \widehat{G}^{ej}(\mathbf{r},\mathbf{r}')\Delta\sigma(\mathbf{r}')\mathbf{\Psi}_n(\mathbf{r}')\, d\mathrm{V}', \quad \mathbf{r} \in \mathbf{R}^3. \tag{25}$$

150 The system matrix in eq. (24) is dense. Thus, as we mentioned above, probably the
151 only way to solve it efficiently when N is large is to use the basis $\{\mathbf{\Psi}_n\}$ which allows for

exploiting the convolution properties (10). Following Kruglyakov & Kuvshinov (2018) we use the piece-wise polynomial basis which is described in Appendix A.

3 IMPLEMENTATION DETAILS

3.1 NIE discretization

Let V be divided into N_c rectangular volume cells, that is

$$\mathrm{V} = \bigcup_{n=1}^{N_c} \mathrm{V}_n^{(c)}, \tag{26}$$

and let $\mathrm{V}^{\mathrm{loc}}$ be divided into N_f rectangular volume cells, that is

$$\mathrm{V}^{\mathrm{loc}} = \bigcup_{n=1}^{N_f} \mathrm{V}_n^{(f),\mathrm{loc}}. \tag{27}$$

We assume that these cells are uniform in lateral directions and the size of $\mathrm{V}_n^{(f),\mathrm{loc}}$ is smaller than that of $\mathrm{V}_n^{(c)}$. We also assume that conductivity distributions in both domains are piece-wise constant functions.

Let further $\left\{\mathbf{\Psi}_{n,k}^{(c)}\right\}, n = 1, 2, \ldots, N_c,\ k = 1, 2, \ldots, K_c$ and $\left\{\mathbf{\Psi}_{n,k}^{(f),\mathrm{loc}}\right\}, n = 1, 2, \ldots, N_f,\ k = 1, 2, \ldots, K_f$ be the piece-wise polynomial bases in V and $\mathrm{V}^{\mathrm{loc}}$, respectively (see Appendix A for details). In this section (and in the appendices) we use the double index n, k for basis functions to stress the fact that

$$\begin{aligned} &\mathrm{supp}\mathbf{\Psi}_{n,k}^{(c)} = \mathrm{V}_n^{(c)} \quad n = 1, 2, \ldots, N_c,\ k = 1, 2, \ldots, K_c, \\ &\mathrm{supp}\mathbf{\Psi}_{m,l}^{(f),\mathrm{loc}} = \mathrm{V}_m^{(f),\mathrm{loc}} \quad m = 1, 2, \ldots, N_f, \quad l = 1, 2, \ldots, K_f. \end{aligned} \tag{28}$$

Thus the first index refers to the space localization of the basis functions, whereas the second one is used to distinguish the basis functions which share the same support.

We can then represent the electric fields in V and $\mathrm{V}^{\mathrm{loc}}$ as

$$\mathbf{E}^{(c)}(\mathbf{r}) = \sum_{n=1}^{N_c} \sum_{k=1}^{K_c} u_{n,k}^{(c)} \mathbf{\Psi}_{n,k}^{(c)}(\mathbf{r}), \quad \mathbf{r} \in \mathrm{V}, \tag{29}$$

$$\mathbf{E}^{(f)}(\mathbf{r}) = \sum_{n=1}^{N_f} \sum_{k=1}^{K_f} u_{n,k}^{(f),\mathrm{loc}} \mathbf{\Psi}_{n,k}^{(f),\mathrm{loc}}(\mathbf{r}), \quad \mathbf{r} \in \mathrm{V}^{\mathrm{loc}}. \tag{30}$$

Using the formalism discussed in the previous section and exploiting representation (29),

eq. (14) is transformed into the system of linear equations for coefficients $u^{(c)}_{n,k}$

$$u^{(c)}_{n,k} - \sum_{m=1}^{N_c}\sum_{l=1}^{K_c} u^{(c)}_{m,l}\left(\mathrm{G_E}\,\Delta\sigma^{(c)}\mathbf{\Psi}^{(c)}_{m,l},\mathbf{\Psi}^{(c)}_{n,k}\right) = \left(\mathbf{E}^0,\mathbf{\Psi}^{(c)}_{n,k}\right), \qquad n=1,2,\ldots,N_c, \quad k=1,2,\ldots,K_c. \tag{31}$$

Similarly, using representation (30), eq. (16) is transformed into the system for coefficients $u^{(f)}_{n,k}$

$$u^{(f),\,\mathrm{loc}}_{n,k} - \sum_{m=1}^{N_f}\sum_{l=1}^{K_f} u^{(f),\,\mathrm{loc}}_{m,l}\left(\mathrm{G_E}\,\Delta\sigma^{(f)}\mathbf{\Psi}^{(f),\,\mathrm{loc}}_{m,l},\mathbf{\Psi}^{(f),\,\mathrm{loc}}_{n,k}\right) = \left(\mathbf{E}^0,\mathbf{\Psi}^{(f),\,\mathrm{loc}}_{n,k}\right) + \left(\mathbf{E}^{add\,(c)},\mathbf{\Psi}^{(f),\,\mathrm{loc}}_{n,k}\right), \qquad n=1,2,\ldots,N_f, \quad k=1,2,\ldots,K_f. \tag{32}$$

Comparing eqs (31) and (32) one can notice that the second term in the right-hand side (RHS) of the equation is a new term. According to eqs (15) and (29), one writes

$$\mathbf{E}^{add\,(c)}(\mathbf{r}) = \sum_{\mathrm{V}^{(c)}_m\subset\mathrm{V}^{\mathrm{out}}}\sum_{l=1}^{K_c}\Delta\sigma^{(c)}_m u^{(c)}_{m,l}\int\limits_{\mathrm{V}^{(c)}_m}\widehat{G}^{ej}(\mathbf{r},\mathbf{r}')\mathbf{\Psi}^{(c)}_{m,l}(\mathbf{r}')d\mathrm{V}^{(c)}_m, \quad \mathbf{r}\in\mathrm{V}^{\mathrm{loc}}. \tag{33}$$

Then the second term of the RHS in eq. (32) becomes

$$\left(\mathbf{E}^{add\,(c)},\mathbf{\Psi}^{(f),\,\mathrm{loc}}_{n,k}\right) = \sum_{\mathrm{V}^{(c)}_m\subset\mathrm{V}^{\mathrm{out}}}\sum_{l=1}^{K_c}\Delta\sigma^{(c)}_m u^{(c)}_{m,l}\int\limits_{\mathrm{V}^{(f),\mathrm{loc}}_n}\int\limits_{\mathrm{V}^{(c)}_m}\mathbf{\Psi}^{(f),\,\mathrm{loc}}_{n,k}(\mathbf{r})\widehat{G}^{ej}(\mathbf{r},\mathbf{r}')\mathbf{\Psi}^{(c)}_{m,l}(\mathbf{r}')d\mathrm{V}^{(c)}_m\,d\mathrm{V}^{(f),\mathrm{loc}}_n, \qquad n=1,2,\ldots,N_f, \quad k=1,2,\ldots,K_f. \tag{34}$$

Now we recall that the sizes of $\mathrm{V}^{(c)}_m$ and $\mathrm{V}^{(f),\,\mathrm{loc}}_n$ are different due to the main idea of the nested approach. Thus in order to calculate the RHS of (34) one has to compute $\mathcal{O}(N_cN_f)$ integrals. This could be computationally very expensive provided N_c and N_f are large. We discuss below how this challenge can be mitigated.

The simplest way to address the problem is to approximate $\mathbf{E}^{add\,(c)}(\mathbf{r})$ in $\mathrm{V}^{\mathrm{loc}}$ as

$$\mathbf{E}^{add\,(c)}(\mathbf{r}) \approx \mathbf{E}^{add\,(c)}_{(c)}(\mathbf{r}) = P_{N^{(c)}}\mathbf{E}^{add\,(c)}(\mathbf{r}) = \sum_{n=1}^{N_c}\sum_{k=1}^{K_c} u^{add\,(c)}_{n,k}\mathbf{\Psi}^{(c)}_{n,k}(\mathbf{r}), \quad \mathbf{r}\in\mathrm{V}^{\mathrm{loc}}, \tag{35}$$

where the coefficients $u_{n,k}^{add\,(c)}$ are calculated – using eq. (33) – as

$$\begin{aligned} u_{n,k}^{add\,(c)} &= \left(\mathbf{E}_{(c)}^{add\,(c)}, \mathbf{\Psi}_{n,k}^{(c)}\right) \\ &= \sum_{\mathrm{V}_m^{(c)} \subset \mathrm{V}^{\mathrm{out}}} \sum_{l=1}^{K_c} \Delta\sigma_m^{(c)} u_{m,l}^{(c)} \int\limits_{\mathrm{V}_n^{(c)}} \int\limits_{\mathrm{V}_m^{(c)}} \mathbf{\Psi}_{n,k}^{(c)}(\mathbf{r}) \widehat{G}^{ej}(\mathbf{r},\mathbf{r}') \mathbf{\Psi}_{m,l}^{(c)}(\mathbf{r}') d\mathrm{V}_m^{(c)}\, d\mathrm{V}_n^{(c)}, \\ &\quad \mathrm{V}_n^{(c)} \subset \mathrm{V}^{\mathrm{loc}}, k = 1, 2, \ldots, K_c. \end{aligned} \tag{36}$$

Since in the above equation only the coarse discretization is involved (which we assume to be laterally-uniform), the coefficients $u_n^{add\,(c)}$ can be efficiently computed by using 2-D FFT. Once these coefficients are calculated, the second term in the RHS of (32) is approximated as

$$\left(\mathbf{E}^{add\,(c)}, \mathbf{\Psi}_{n,k}^{(f),\mathrm{loc}}\right) \approx \sum_{\mathrm{V}_m^{(c)} \subset \mathrm{V}^{\mathrm{loc}}} \sum_{l=1}^{K_c} u_{m,l}^{add\,(c)} \int\limits_{\mathrm{V}_n^{(f),\mathrm{loc}}} \mathbf{\Psi}_{n,k}^{(f),\mathrm{loc}}(\mathbf{r}) \mathbf{\Psi}_{m,l}^{(c)}(\mathbf{r}) d\mathrm{V}_n^{(f),\mathrm{loc}}, \tag{37}$$
$$n = 1, 2, \ldots, N_f, \quad k = 1, 2, \ldots, K_f.$$

Note that integrals in the latter equation (which are just the projection coefficients from one basis to another) can be computed analytically (see Appendix B).

However, our numerical experiments (see Section 4.1) show that such an approach to calculating $\left(\mathbf{E}^{add\,(c)}, \mathbf{\Psi}_n^{(f),\mathrm{loc}}\right)$ leads to large artifacts in the IE solution in $\mathrm{V}^{\mathrm{loc}}$. These artifacts come from the following phenomenon. As seen, for instance, from eq. (15), $\mathbf{E}^{add\,(c)}$ is a field induced by a current occupied the domain $\mathrm{V}^{\mathrm{out}}$. This, in particular, means that $\mathbf{E}^{add\,(c)}$ changes abruptly when $\mathbf{r}$ is close to $\mathbf{r}'$, i.e. near the boundaries of the domain $\mathrm{V}^{\mathrm{loc}}$. This is due to the "singular" behavior of tensor $\widehat{G}^{ej}$ when $\mathbf{r}$ tends to $\mathbf{r}'$. Hence the "coarse" approximation of $\mathbf{E}^{add\,(c)}$ by $\mathbf{E}_{(c)}^{add\,(c)}$ introduces substantial errors in $\mathbf{E}^{add\,(c)}$, which in turn leads to the errors in the final results. Below we explain the numerical recipe which allows us to overcome this problems, while still exploiting the (efficient) scheme of estimating $\mathbf{E}^{add\,(c)}$ described above.

3.2 Rim domain concept (RDC)

Let us introduce domain $\mathrm{V}^{\mathrm{loc}+}$ such that $\mathrm{V}^{\mathrm{loc}} \subset \mathrm{V}^{\mathrm{loc}+} \subset \mathrm{V}$, as shown in Figure 2. We denote this domain as $\mathrm{V}^{\mathrm{loc}+}$ to emphasize the fact that it is insignificantly larger than $\mathrm{V}^{\mathrm{loc}}$.

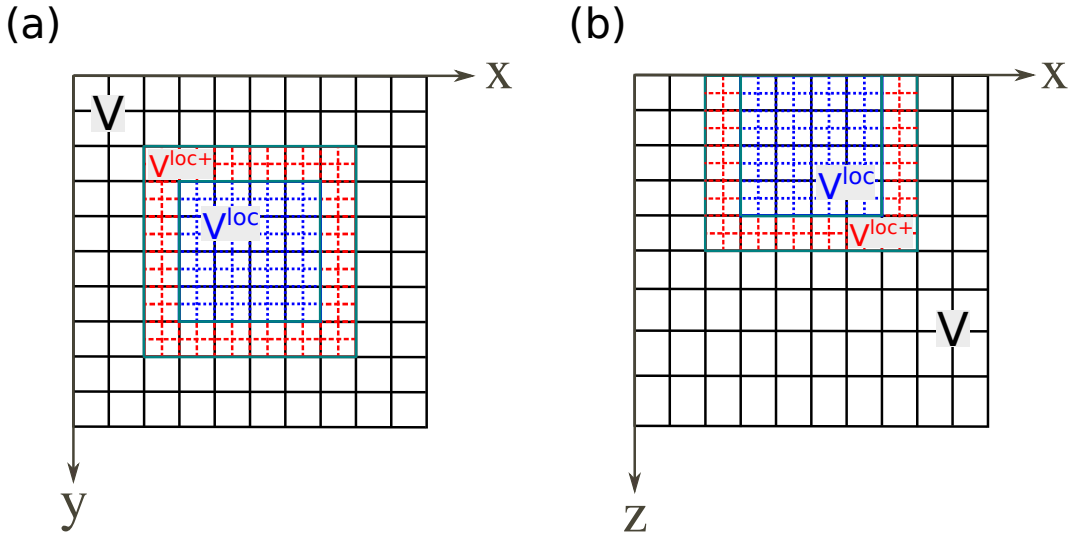

Figure 2. Illustration of the rim domain concept, which is introduced to avoid the boundary effect in the nested IE approach: (a) a top view, and (b) the cross section. $\mathrm{V}^{\mathrm{loc}+}$ comprises $\mathrm{V}^{\mathrm{loc}}$ and an additional "narrow" rim (a few coarse grid cells in width), i.e. $\mathrm{V}^{\mathrm{loc}+} = \mathrm{V}^{\mathrm{loc}} \bigcup \mathrm{V}^{\mathrm{rim}}$. See details in the text.

How large this domain has to be taken will be explained below. We also denote as $\mathrm{V}^{\mathrm{rim}}$ the complement of $\mathrm{V}^{\mathrm{loc}}$ to $\mathrm{V}^{\mathrm{loc}+}$, i.e.

$$\mathrm{V}^{\mathrm{rim}} = \mathrm{V}^{\mathrm{loc}+} \setminus \mathrm{V}^{\mathrm{loc}}, \tag{38}$$

and denote as $\mathrm{V}^{\mathrm{ext}}$ the complement of $\mathrm{V}^{\mathrm{loc}+}$ to V, i.e.

$$\mathrm{V}^{\mathrm{ext}} = \mathrm{V} \setminus \mathrm{V}^{\mathrm{loc}+}. \tag{39}$$

Then $\mathbf{E}^{add\,(c)}$ can be written as

$$\mathbf{E}^{add\,(c)}(\mathbf{r}) = \mathbf{E}^{add\,(c)}_{ext}(\mathbf{r}) + \mathbf{E}^{add\,(c)}_{rim}(\mathbf{r}), \quad \mathbf{r} \in \mathrm{V}^{\mathrm{loc}}, \tag{40}$$

where, in accordance with (15), $\mathbf{E}^{add\,(c)}_{ext}$ and $\mathbf{E}^{add\,(c)}_{rim}$ read

$$\mathbf{E}^{add\,(c)}_{ext}(\mathbf{r}) = \int\limits_{\mathrm{V}^{\mathrm{ext}}} \widehat{G}^{ej}(\mathbf{r},\mathbf{r}')\Delta\sigma^{(c)}(\mathbf{r}')\mathbf{E}^{(c)}(\mathbf{r}')d\mathrm{V}, \quad \mathbf{r} \in \mathrm{V}^{\mathrm{loc}}, \tag{41}$$

$$\mathbf{E}^{add\,(c)}_{rim}(\mathbf{r}) = \int\limits_{\mathrm{V}^{\mathrm{rim}}} \widehat{G}^{ej}(\mathbf{r},\mathbf{r}')\Delta\sigma^{(c)}(\mathbf{r}')\mathbf{E}^{(c)}(\mathbf{r}')d\mathrm{V}, \quad \mathbf{r} \in \mathrm{V}^{\mathrm{loc}}. \tag{42}$$

The idea behind splitting the integral over domain $\mathrm{V}^{\mathrm{out}}$ onto integrals over "rim domain" $\mathrm{V}^{\mathrm{rim}}$ and "external" domain $\mathrm{V}^{\mathrm{ext}}$ is as follows. If the distance between boundaries of the

$\mathrm{V}^{\mathrm{ext}}$ and $\mathrm{V}^{\mathrm{loc}}$ (i.e. distance between $\mathbf{r}$ and $\mathbf{r}'$ in integral (41)) is large enough, then function $\mathbf{E}^{add\,(c)}_{ext}(\mathbf{r}), \mathbf{r} \in \mathrm{V}^{\mathrm{loc}}$ can be approximated by using the "coarse" basis $\mathbf{\Psi}^{(c)}$ as described above, because in this case $\mathbf{E}^{add\,(c)}_{ext}(\mathbf{r})$ does not undergo abrupt changes. Note, that our numerical experiments (to be discussed in the next section) demonstrate that a "large enough" distance between boundaries of $\mathrm{V}^{\mathrm{ext}}$ and $\mathrm{V}^{\mathrm{loc}}$ (i.e. the distance between external boundaries of $\mathrm{V}^{\mathrm{loc+}}$ and $\mathrm{V}^{\mathrm{loc}}$) is achieved when they are separated by one or two coarse cells in the corresponding direction.

Ultimately we have to solve the system (32) and thus calculate

$$\left(\mathbf{E}^{add\,(c)}, \mathbf{\Psi}^{(f),\,\mathrm{loc}}_{n,k}\right) = \left(\mathbf{E}^{add\,(c)}_{ext}, \mathbf{\Psi}^{(f),\,\mathrm{loc}}_{n,k}\right) + \left(\mathbf{E}^{add\,(c)}_{rim}, \mathbf{\Psi}^{(f),\,\mathrm{loc}}_{n,k}\right), \qquad n = 1, 2, \ldots, N_f, \quad k = 1, 2, \ldots, K_f. \tag{43}$$

As we already mentioned above, to calculate the first term in the RHS of the latter equation we make use of eq. (37), namely

$$\left(\mathbf{E}^{add\,(c)}_{ext}, \mathbf{\Psi}^{(f),\,\mathrm{loc}}_{n,k}\right) \approx \sum_{\mathrm{V}^{(c)}_m \subset \mathrm{V}^{\mathrm{ext}}} \sum_{l=1}^{K_c} u^{add\,(c)}_{m,l} \int\limits_{\mathrm{V}^{(f),\,\mathrm{loc}}_n} \mathbf{\Psi}^{(f),\,\mathrm{loc}}_{n,k}(\mathbf{r}) \mathbf{\Psi}^{(c)}_{m,l}(\mathbf{r}) d\mathrm{V}^{(f),\,\mathrm{loc}}_n, \qquad n = 1, 2, ..., N_f, \quad k = 1, 2, \ldots, K_f. \tag{44}$$

To calculate the second term in the RHS of (43) we propagate our "fine" basis $\left\{\mathbf{\Psi}^{(f),\,\mathrm{loc}}_{n,k}\right\}$ from domain $\mathrm{V}^{\mathrm{loc}}$ to domain $\mathrm{V}^{\mathrm{loc+}}$. This can be done by using the same (fine) discretization in $\mathrm{V}^{\mathrm{loc+}}$ as in $\mathrm{V}^{\mathrm{loc}}$ and taking into account that local basis functions are the same for different cells (see Appendix A). Now, we can project $\mathbf{E}^{(c)}(\mathbf{r}), \mathbf{r} \in \mathrm{V}^{\mathrm{loc+}}$ from the coarse $\left\{\mathbf{\Psi}^{(c)}_{n,k}\right\}$ to the fine $\left\{\mathbf{\Psi}^{(f),\,\mathrm{loc}}_{m,l}\right\}$ basis (see Appendix B for details) as

$$\mathbf{E}^{(c)}(\mathbf{r}) \approx \sum_{n=1}^{N_{loc+}} \sum_{k=1}^{K_f} u^{loc+}_{n,k} \mathbf{\Psi}^{(f),\,\mathrm{loc}}_{n,k}(\mathbf{r}), \tag{45}$$

substitute it into eq. (42), and then into the second term of eq. (43) thus obtaining

$$\left(\mathbf{E}^{add\,(c)}_{rim}, \mathbf{\Psi}^{(f),\,\mathrm{loc}}_{n,k}\right) \approx \sum_{\mathrm{V}^{(f),\,\mathrm{loc}}_m \subset \mathrm{V}^{\mathrm{rim}}} \sum_{l=1}^{K_f} \Delta\sigma^{(f)}_m u^{loc+}_{m,l} \int\limits_{\mathrm{V}^{(f),\mathrm{loc}}_n} \int\limits_{\mathrm{V}^{(f),\mathrm{loc}}_m} \mathbf{\Psi}^{(f),\,\mathrm{loc}}_{n,k}(\mathbf{r}) \widehat{G}^{ej}(\mathbf{r}, \mathbf{r}') \mathbf{\Psi}^{(f),\,\mathrm{loc}}_{m,l}(\mathbf{r}') d\mathrm{V}^{(f),\mathrm{loc}}_m \, d\mathrm{V}^{(f),\mathrm{loc}}_n, \qquad n = 1, 2, ..., N_f, \quad k = 1, 2, \ldots, K_f. \tag{46}$$

One can see that to obtain the RHS of the latter equation one has to compute only $\mathcal{O}(N_f)$ integrals, since $\mathrm{V}^{\mathrm{rim}}$ is small compared to $\mathrm{V}^{\mathrm{loc}}$.

4 NUMERICAL TESTS

To verify the developed nested IE tool, we performed the tests in two 3-D conductivity models.

4.1 3D-2 model

The first (3D-2) model comes from COMMEMI project (Zhdanov et al. 1997), which is widely used to validate the newly developed EM modeling solvers (Mitsuhata & Uchida 2004; Ren et al. 2014; Grayver & Bürg 2014; Kruglyakov & Kuvshinov 2018, among others). The model comprises two – relatively resistive and relatively conductive – blocks embedded in the three-layered background. The side and plane views of the model, as well as the resistivities assigned to the different structures, are shown in Figure 3.

The reference ("true") results are computed by using the IE-based solver PGIEM2G (Kruglyakov & Kuvshinov 2018) on a "fine grid" in the whole domain V (which is depicted as a black rectangle in Figure 3). Three comments are relevant at this point: a) the presented nested IE tool uses the core modules of the PGIEM2G solver; b) the PGIEM2G solver itself was successfully verified against the FEM-based solver by Grayver & Kolev (2015); c) as in Kruglyakov & Kuvshinov (2018) (where the same model was also used for the testing purpose), in all model experiments of this section the same (3rd) order of polynomial basis was used in both lateral and vertical directions. Table 1 presents the number of cells and their sizes for the reference IE modeling, and for two numerical experiments using the two-step nested IE approach. Note that the goal of these two numerical experiments is two-fold: first, to validate the nested approach, and second, to show that one indeed has to use the rim domain concept (RDC) in order to obtain the correct results.

For the "nested" computations we take the central, shallow part of the model $\mathrm{V}^{\mathrm{loc}}$ as a local domain; it is depicted as a blue rectangle in Figure 3. $\mathrm{V}^{\mathrm{loc}}$ occupies a $20 \times 15 \times 0.5$ km^3 vol-

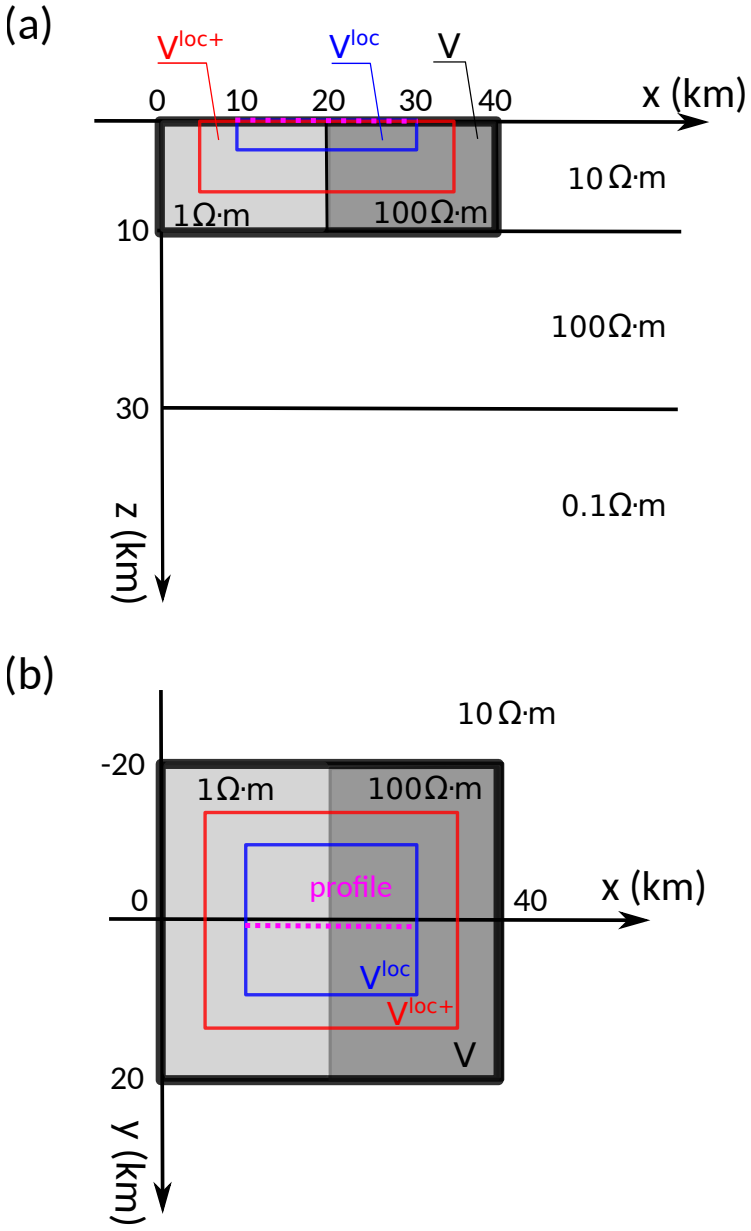

Figure 3. The 3D-2 model from the COMMEMI project (Zhdanov et al. 1997): (a) a side view of the model and (b) a plan view. V represents the whole modeling domain, V^{loc} denotes the local domain, and domain V^{loc+} comprises V^{loc} and the additional (narrow) rim (of width of a few coarse grid cells), i.e. $V^{loc+} = V^{loc} \bigcup V^{rim}$. Dashed pink line denotes the profile at the Earth's surface at which the modeling results are presented.

ume. The domain $V^{loc+} \equiv V^{loc} \cup V^{rim}$ is depicted by the red line in Figure 3; the rim's width is taken as one coarse cell in y-direction and two coarse cells in both x- and z-directions.

The results of our model experiments are summarized in Figures 4 - 7. The figures present the computed apparent resistivities and phases of MT impedances (Chave & Jones

Table 1. Number of cells and their sizes for the reference IE calculations, and for the numerical experiments using the two-step nested NIE approach.

	$N_x \times N_y \times N_z$	$dx \times dy$	dz
Reference (conventional) IE (at V)	$64 \times 16 \times 4$	$0.625 \times 2.5\,\mathrm{km}^2$	$0.5, 0.5, 4, 5$ km
1st step of NIE (at V)	$16 \times 16 \times 4$	$2.5 \times 2.5\,\mathrm{km}^2$	$0.5, 0.5, 4, 5$ km
2nd step of NIE (at $\mathrm{V}^{\mathrm{loc}}$, using RDC)	$24 \times 8 \times 3$	$1.25 \times 2.5\,\mathrm{km}^2$	$0.5, 0.5, 4$ km
2nd step of NIE (at $\mathrm{V}^{\mathrm{loc}}$, not using RDC)	$16 \times 6 \times 1$	$1.25 \times 2.5\,\mathrm{km}^2$	0.5 km

2012) at periods of 10 and 1000 sec along the profile shown in Figure 3. One can see that the responses calculated by using the nested approach using RDC (red stars) match well with the "true" responses (black line). The relative differences for the off-diagonal apparent

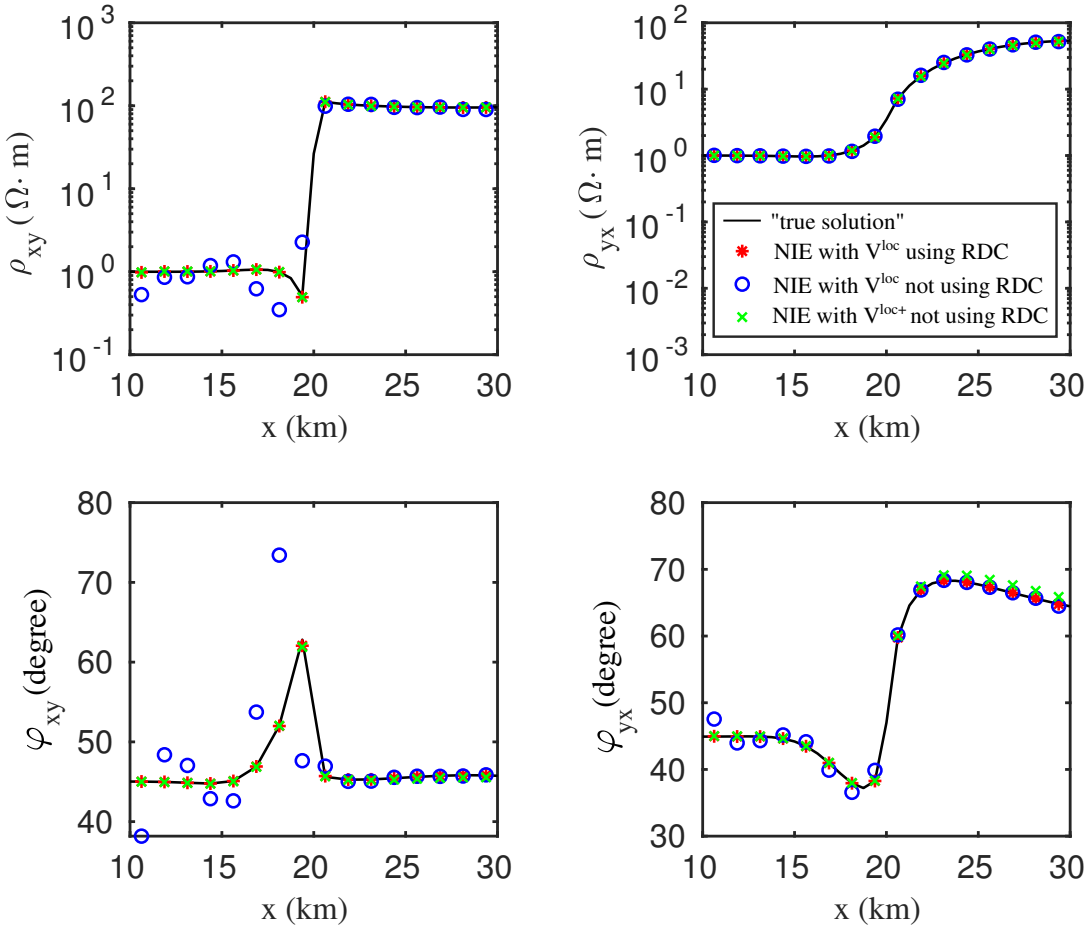

Figure 4. Apparent resistivities (ρ_{xy} and ρ_{yx}) and phases (φ_{xy} and φ_{yx}) of MT impedance at the period of 10 sec along the profile shown in Figure 3. The results are for the reference modeling and for three scenarios of two-step NIE. See details in the text.

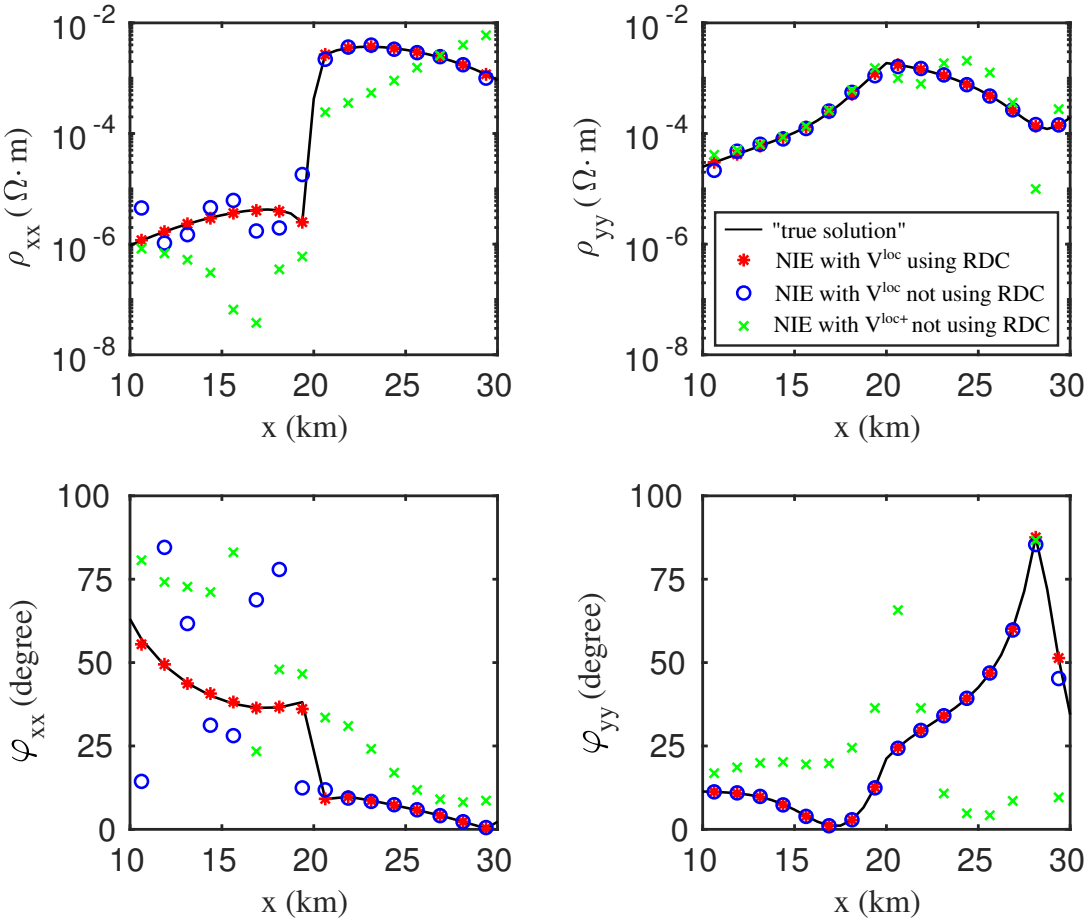

Figure 5. As in Figure 4, but for apparent resistivities (ρ_{xx} and ρ_{yy}) and phases (φ_{xx} and φ_{yy}).

resistivities are smaller than 3 %, and the differences in the phases are smaller than 0.25 degree (cf. Figures 8 - 9).

At the same time, the responses computed by the nested approach, but without considering RDC (blue circles) noticeably differ from the "true" responses (see again Figures 4 -7). These results clearly demonstrate the importance of using the RDC.

However, invoking the RDC makes the implementation of the nested approach more complicated. In this context the natural question arises whether one can avoid using the RDC by just increasing the size of the local domain? This seems feasible, especially when the modeler is interested in the results only in the central part of the local domain, i.e. far from its boundaries. Indeed, it is quite obvious that if the local domain is taken large enough, there is no need to use the RDC. But the usage of a large local domain contradicts

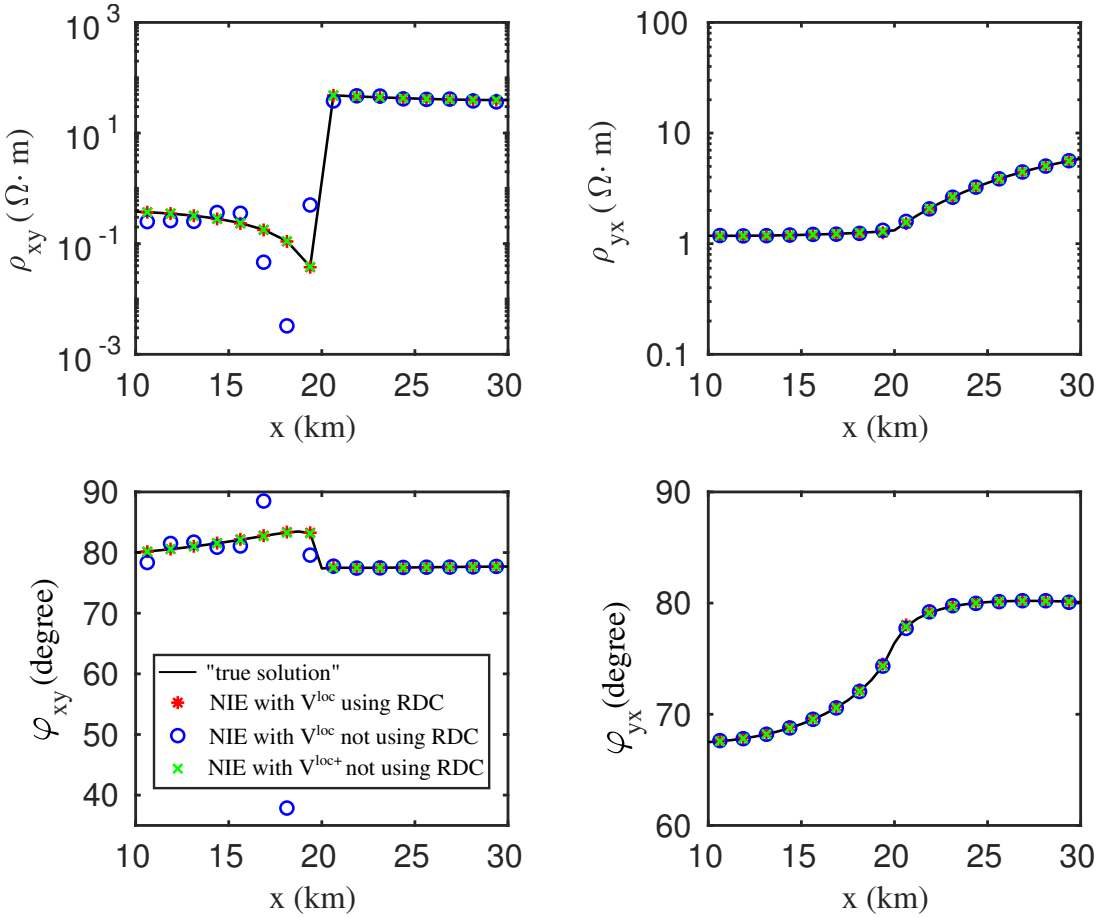

Figure 6. As in Figure 4, but at the period of 1000 sec.

the idea of the nested approach, namely, minimization of the computational loads by making the local domain as small as practicable.

To explore further the importance of using the RDC, we performed the nested modeling in which the local domain is extended to V^{loc+} (and no rim domain is invoked). The results are shown in Figures 4 - 7 by green crosses. One can see a good agreement of the obtained responses with "true" responses in the off-diagonal components (Figures 4 and 6). However, the agreement in the diagonal components (Figures 5 and 7) appeared to be poor.

Next, two model experiments further advocate using the RDC. The first experiment involves three-step nested IE modeling without considering the rim domain. The number of cells and their sizes for the performed computations are listed in Table 2. The first-step IE modeling is the same as that in the two-step implementation discussed above. In the second and the third steps, the regions V^{loc+} and V^{loc} were chosen as the local domains.

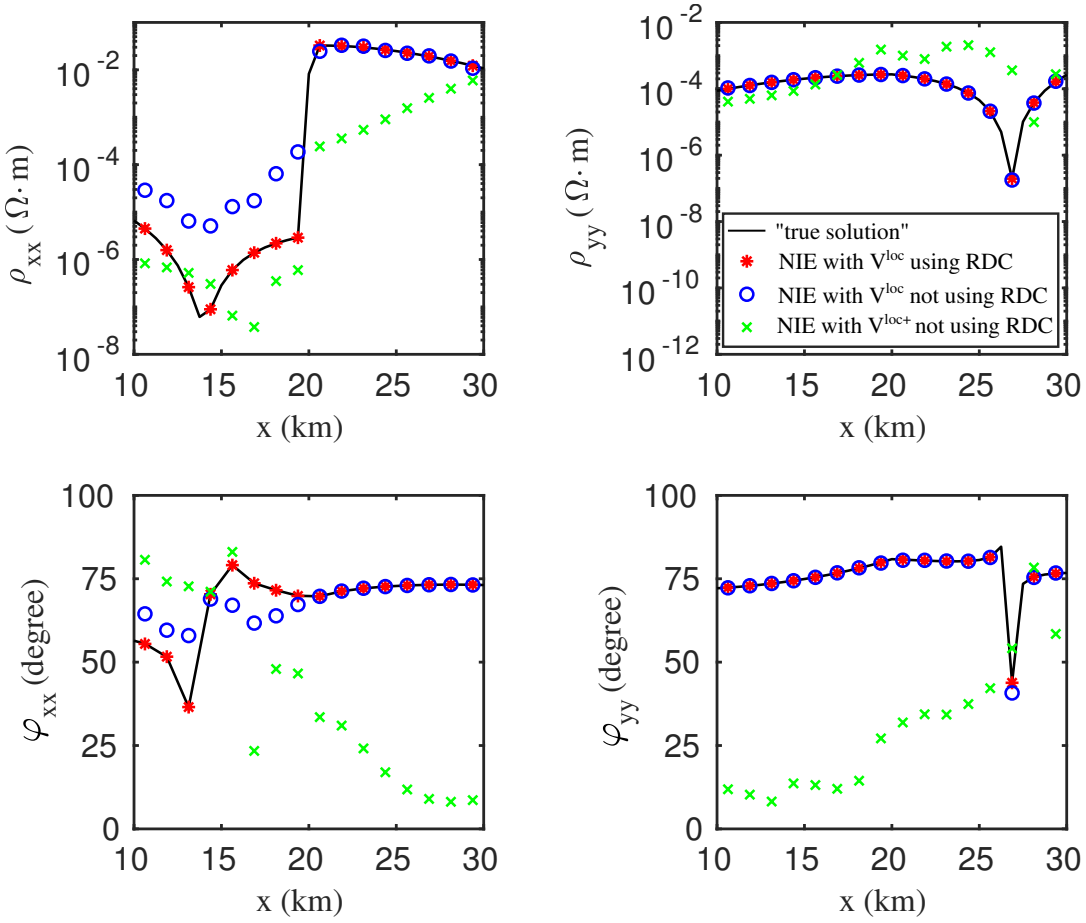

Figure 7. As in Figure 5, but at the period of 1000 sec.

As is seen from Figure 10, the off-diagonal components in the local domain computed at the second-step IE modeling match well with the "true" solutions – as expected, according to the previous results. However, the third step destroys this agreement for ρ_{xy} and φ_{xy}, especially at the interface of two anomalous blocks and the boundary of the local domain.

Table 2. Number of cells and their sizes for the numerical experiment using a three-step NIE approach without invoking RDC.

	$N_x \times N_y \times N_z$	$dx \times dy$	dz
1st step of NIE (at V)	$16 \times 16 \times 4$	$2.5 \times 2.5\,\mathrm{km}^2$	$0.5, 0.5, 4, 5$ km
2nd step of NIE (at V^{loc+})	$24 \times 8 \times 3$	$1.25 \times 2.5\,\mathrm{km}^2$	$0.5, 0.5, 4$ km
3rd step of NIE (at V^{loc})	$32 \times 6 \times 1$	$0.625 \times 2.5\,\mathrm{km}^2$	0.5 km

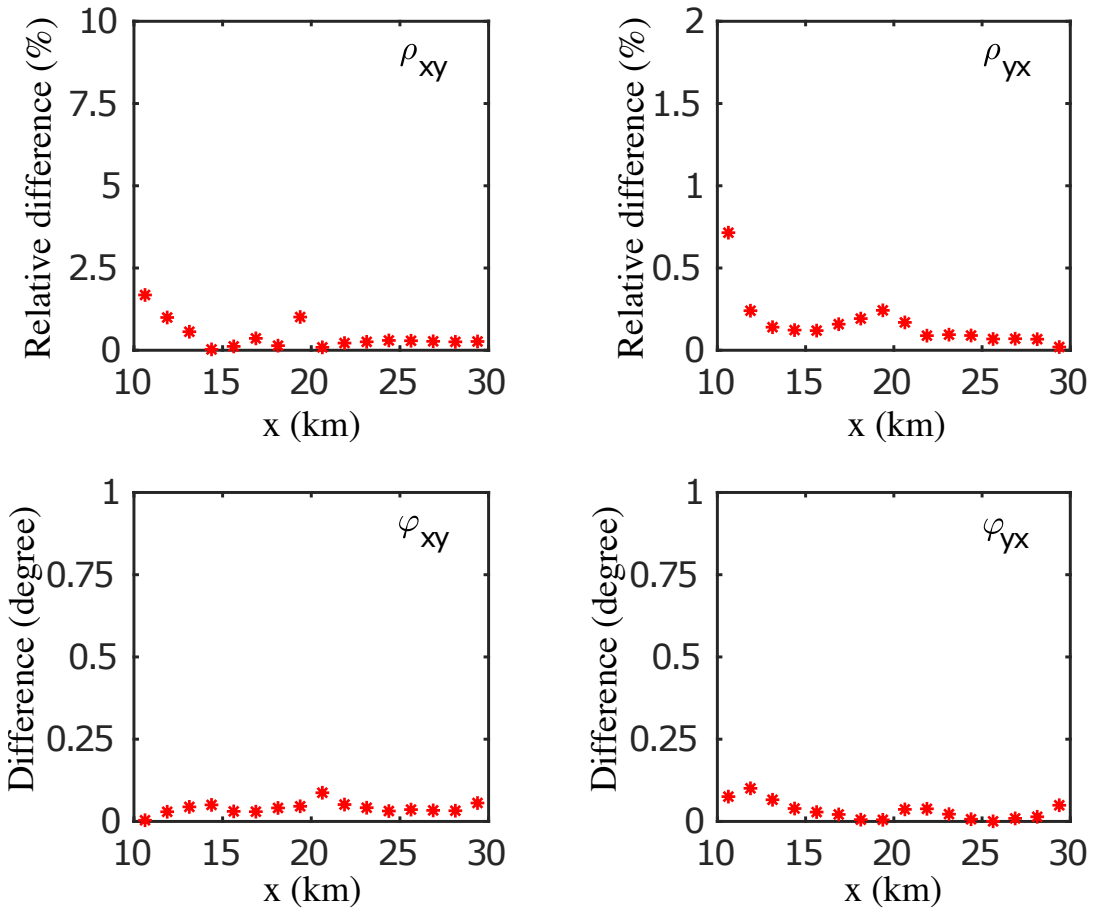

Figure 8. Top row: relative differences between "true" off-diagonal apparent resistivities and those calculated using NIE. Bottom row: differences in the off-diagonal phases of impedance. The results are for a period of 10 sec.

The reason for this is that the RHS at the third step is an integral over the $\mathrm{V}^{\mathrm{loc}+} \setminus \mathrm{V}^{\mathrm{loc}}$ i.e. over the domain where the solution at the second step has the largest errors.

As a final model experiment we performed the three-step RDC-based nested modeling. At the second step, one coarse cell in the y, z-directions and two coarse cells in the x-direction were considered as the rim domain, while one coarse cell in the y-direction and two coarse cells were considered in the x, z-directions at the third step. The lateral discretization used in this experiment is exactly the same as the one in the three-step nested modeling without considering RDC. Very good agreement between the responses based on the three-step nested IE (red stars in the Figure 10) and the "true" responses is now observed. This

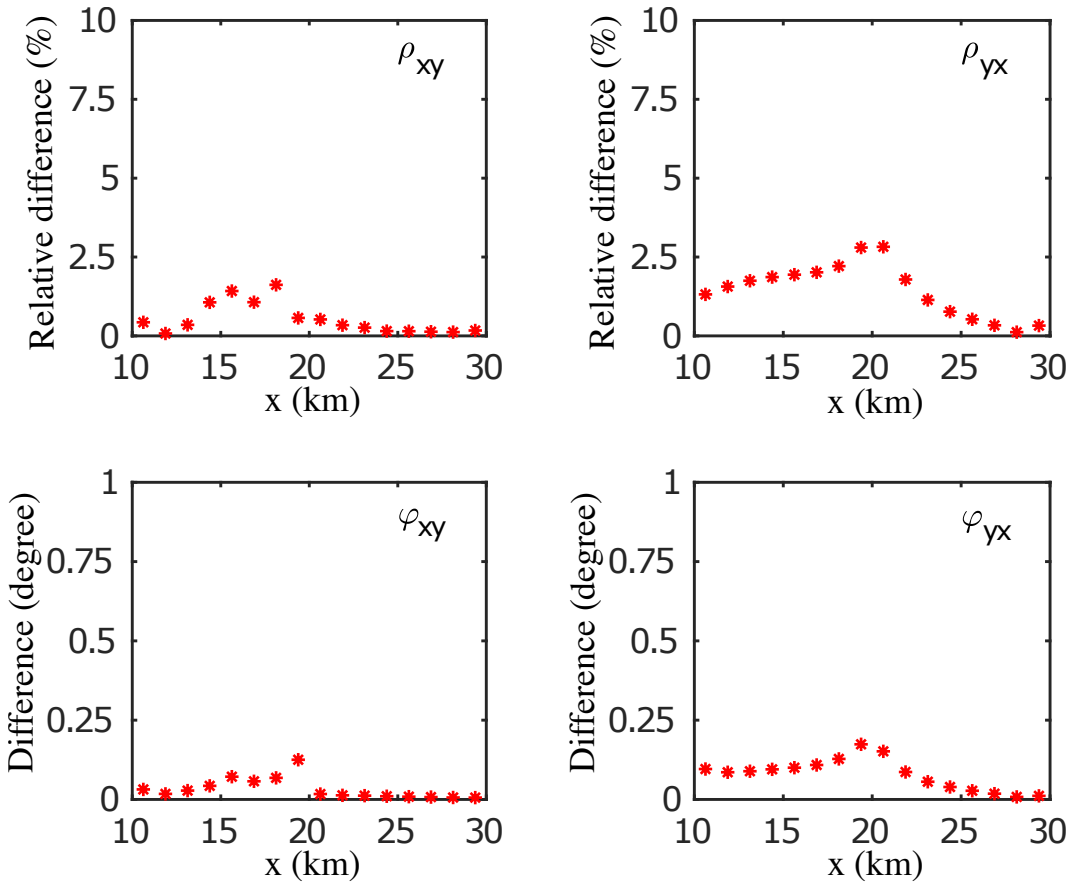

Figure 9. As in Figure 8, but for the period of 1000 sec.

demonstrates again that the usage of the RDC is essential for obtaining accurate results in the local domain, especially for the multi-step realization of the nested IE approach.

4.2 Realistic conductivity model around Gan geomagnetic observatory

The second test aims to illustrate the ability of the nested tool to deal with the realistic conductivity models, where both the distant non-uniform structures and the local bathymetry have to be taken into account. Our previous study (Chen et al. 2020) shows that the responses of islands at periods longer than a few days (Banks 1969) are strongly affected by the ocean induction effect, which can be accounted for by using the high-resolution bathymetry and a nested approach. Here we look at the shorter-period island responses, namely, magnetic MT transfer functions (tippers) that relate the vertical magnetic field, H_z, with the

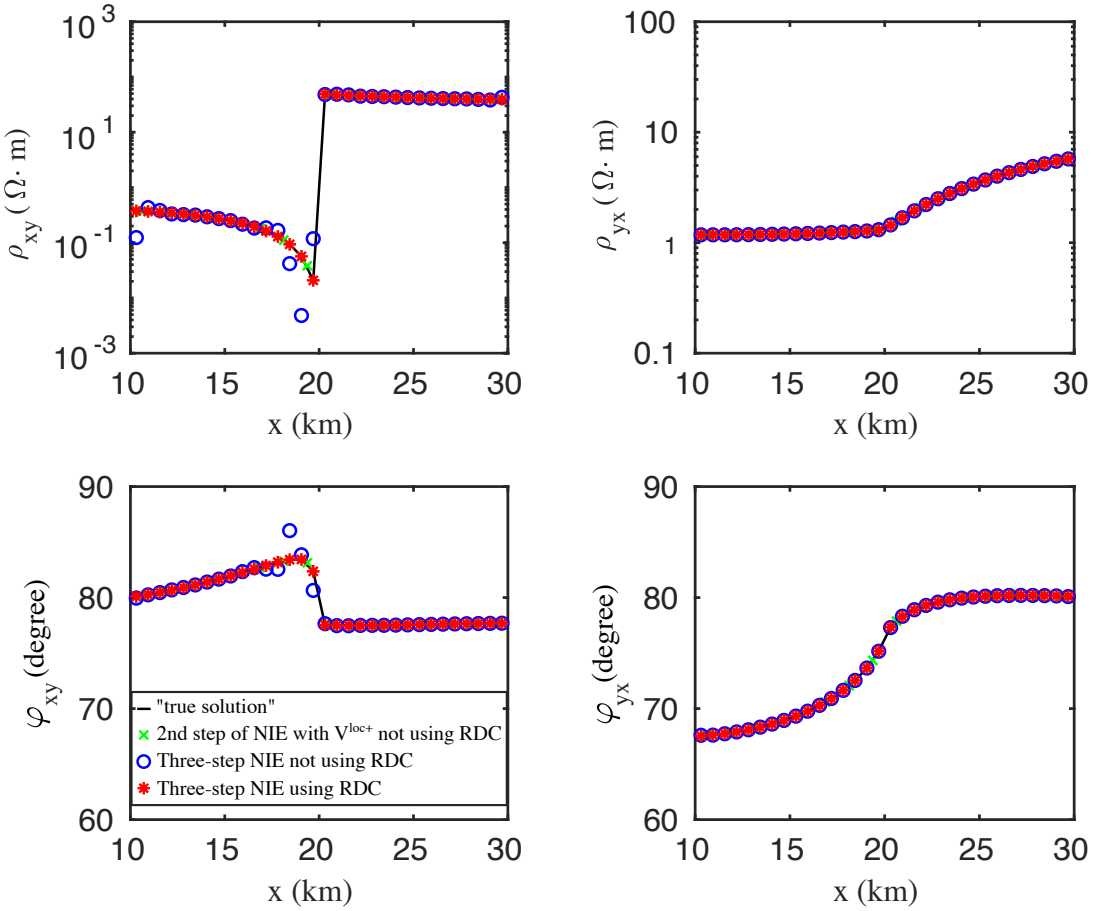

Figure 10. Apparent resistivities (ρ_{xy} and ρ_{yx}) and phases (φ_{xy} and φ_{yx}) of MT impedance at the period of 1000 sec along the profile shown in Figure 3. The results are for the reference modeling and for three scenarios of three-step NIE. See details in the text.

horizontal magnetic field, $\mathbf{H}_\tau$

$$H_z(\mathbf{r}_s,\omega) = T(\mathbf{r}_s,\omega)\mathbf{H}_\tau(\mathbf{r}_s,\omega), \quad T = [T_{zx} \quad T_{zy}]. \tag{47}$$

As an island geomagnetic observatory we consider the observatory Gan located at the southernmost island of the Maldives archipelago (longitude: 73.1537° E; latitude: 0.6946° S; INTERMAGNET code: GAN). The realistic conductivity model consists of a 1-D Earth's conductivity overlaid by an oceanic layer with a 3-D conductivity distribution. The 1-D conductivity (shown in Figure 11a) is taken from Morschhauser et al. (2019), whereas the 3-D conductivity distribution is constructed by using the $30'' \times 30''$ bathymetry data from the General Bathymetry Chart of the Oceans (GEBCO; Becker et al. (2009)); note that $30'' \times 30''$ (spherical) resolution corresponds to $\approx 0.9 \times 0.9$ km^2 resolution at the equator. Laterally, the

domain V is confined to $70.66° - 75.66°$ longitudes and $-3.20° - 1.80°$ latitudes. Bathymetry in this region is shown in Figure 11b. In order to obtain the bathymetry distribution in Cartesian coordinates, the Mercator map projection as described in Snyder (1982) is employed. Eventually, the modeling domain V occupies the volume of $555 \times 555 \times 5.5$ $(x \times y \times z)$ km^3. Furthermore, the obtained bathymetry is used for the construction of 3-D conductivity distribution in the model. We also used a (much) higher-resolution coastline database (of resolution of $\approx 60 \times 60$ m^2 in GAN region) from the Global Self-consistent, Hierarchical, High-resolution Geography Database (GSHHG) (Wessel & Smith 1996; Bohlander & Scambos 2007) in order to correct the bathymetry-based model when constructing a high resolution 3-D conductivity model in the local domain. The conductivities of seawater are obtained from the World Ocean Atlas at the $1° \times 1°$ resolution and are available in the supplementary material of Grayver et al. (2016). The conductivity within the cells that contain the land-seawater interface is computed as the depth-integrated average. Gan island is very flat, thus the topography is not included in the model. The constructed 3-D conductivity model is shown in Figure 12.

In this model experiment, we compare tippers computed using the NIE and FEM solvers. The FEM results are from Morschhauser et al. (2019); in that paper the authors used the FEM solver of Grayver & Kolev (2015) to model the GAN tippers.

NIE modeling was performed using the three-step scheme. Table 3 summarizes the details (number and sizes of cells) for each NIE step. We note here that the highest NIE resolution ($61.7 \times 61.7 \times 15$ m^3 at the third step) was made comparable with the highest resolution of FEM modeling ($62.5 \times 62.5 \times 15.6$ m^3). We also notice that the rim domain at the second and third steps of NIE had a width of two cells (from the previous step) in all directions. Final comment on the NIE modeling set up is that we adopted the first order polynomial basis for all steps, assuming that the cell's sizes (at least at the second and the third steps) are small enough not to consider a higher-order polynomial basis.

Figure 13 presents the modeled tippers at 16 periods from 10 to 10000 sec. In addi-

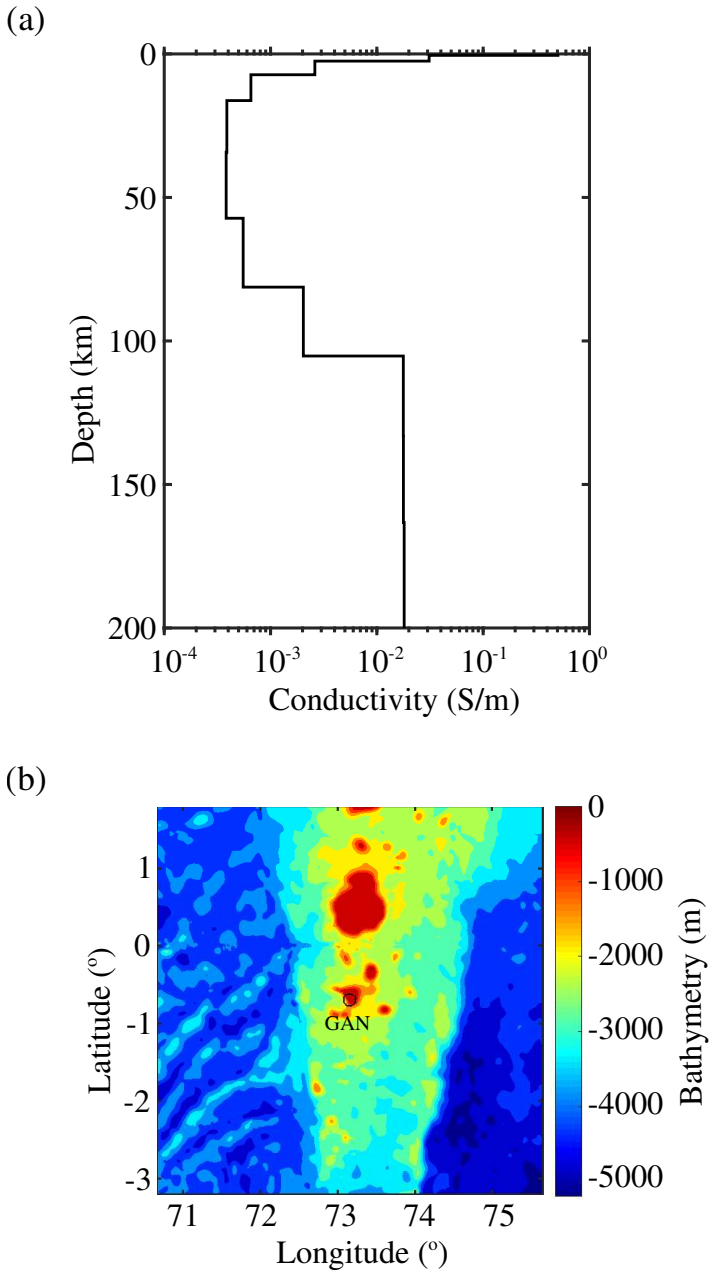

Figure 11. (a) 1-D conductivity profile beneath GAN observatory; (b) Bathymetry distribution in the vicinity of the GAN geomagnetic observatory.

tion, the figure demonstrates the observed (i.e. estimated from the data) tippers and their uncertainties.

It is seen from the figure that NIE- and FEM-based tippers agree (within experimental uncertainties) at all periods in both components and in both real and imaginary parts. It is important to stress that we did not expect an "ideal" fit, since we cannot make the

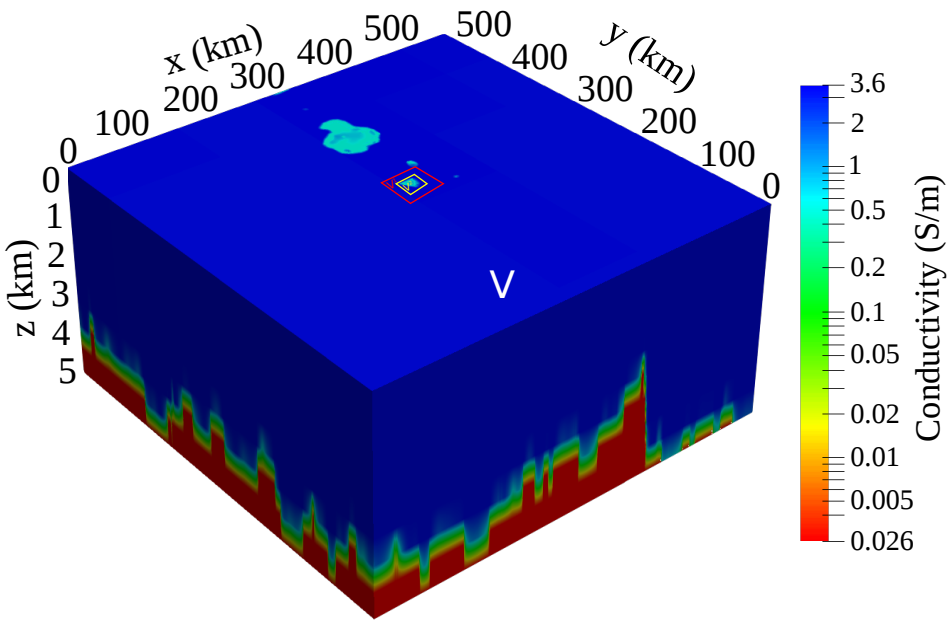

Figure 12. 3-D view of conductivity distribution in the domain V of the GAN model. Red and yellow rectangles depict lateral size of the V^1 and V^2 domains, respectively.

Table 3. Number of cells and their sizes in three-step NIE modeling in the GAN model.

	$N_x \times N_y \times N_z$	$dx \times dy$	dz
1st step of NIE (at V)	$600 \times 600 \times 10$	$926 \times 926\,\mathrm{m}^2$	5×500, 5×600 m
2nd step of NIE (at V^1)	$380 \times 380 \times 4$	$185 \times 185\,\mathrm{m}^2$	15, 35, 150, 300 m
3rd step of NIE (at V^2)	$588 \times 588 \times 4$	$61.7 \times 61.7\,\mathrm{m}^2$	15, 35, 150, 300 m

Table 4. Computational loads (memory and CPU time) used for three-step NIE modeling in the GAN model. The computational time is the averaged time for the simulation at one period and for one plane wave excitation. Computations are performed using 600 CPUs. Computational loads for the conventional IE method (at V, and a fine grid corresponding to the NIE 3rd step resolution) are estimated without actual computations; this is due to the fact that such modeling would require enormous computational resources.

	RAM (GB)	Wall time (sec)
Nested IE approach	146	543
Conventional IE, fine	5.6×10^4	1.6×10^5

conductivity distributions identical due to the substantially different grids used by NIE and FE solvers.

It is noteworthy that both NIE- and FEM-based results for the real part of T_{zy} differ from the observed tippers. As pointed out by Morschhauser et al. (2019) the noticeable disagreement may result from 3-D conductivity structures that are incompatible with the assumed 1-D model beneath the ocean, for example, due to conductive seafloor sediments at some distance from the station, or to inaccuracies of the bathymetry model.

Lastly, Table 4 illustrates one of the most significant results of the paper: remarkable computational efficiency of the developed nested IE. As is seen from the table, the nested IE modeling significantly outperforms the modeling based on the most advanced conventional IE solver (Kruglyakov & Kuvshinov 2018) in terms of memory and CPU time.

5 CONCLUDING REMARKS

We have developed an efficient and accurate 3-D EM modeling tool based on an IE approach with multi-nested domains. We successfully verify the workability and accuracy of the developed nested IE tool by performing modelings in both idealized and realistic 3-D conductivity models. We demonstrate that the new tool is two orders of magnitude more efficient – in terms of both memory and CPU time – than one of the most advanced conventional IE solvers (Kruglyakov & Kuvshinov 2018).

An important novelty of the paper is a development of the "rim domain" concept which further improves the efficiency of the multi-nested IE approach.

The developed tool, in combination with the global-to-Cartesian EM modeling tool (Chen et al. 2020), which aims to efficiently model longer-period responses, gives us an opportunity to invert EM responses in as wide a range of periods as practicable, and thus to constrain the electrical structure of the Earth's interior from the crust to the middle mantle.

ACKNOWLEDGMENTS

The authors acknowledge GEBCO Compilation Group (2014), who provided accurate high-

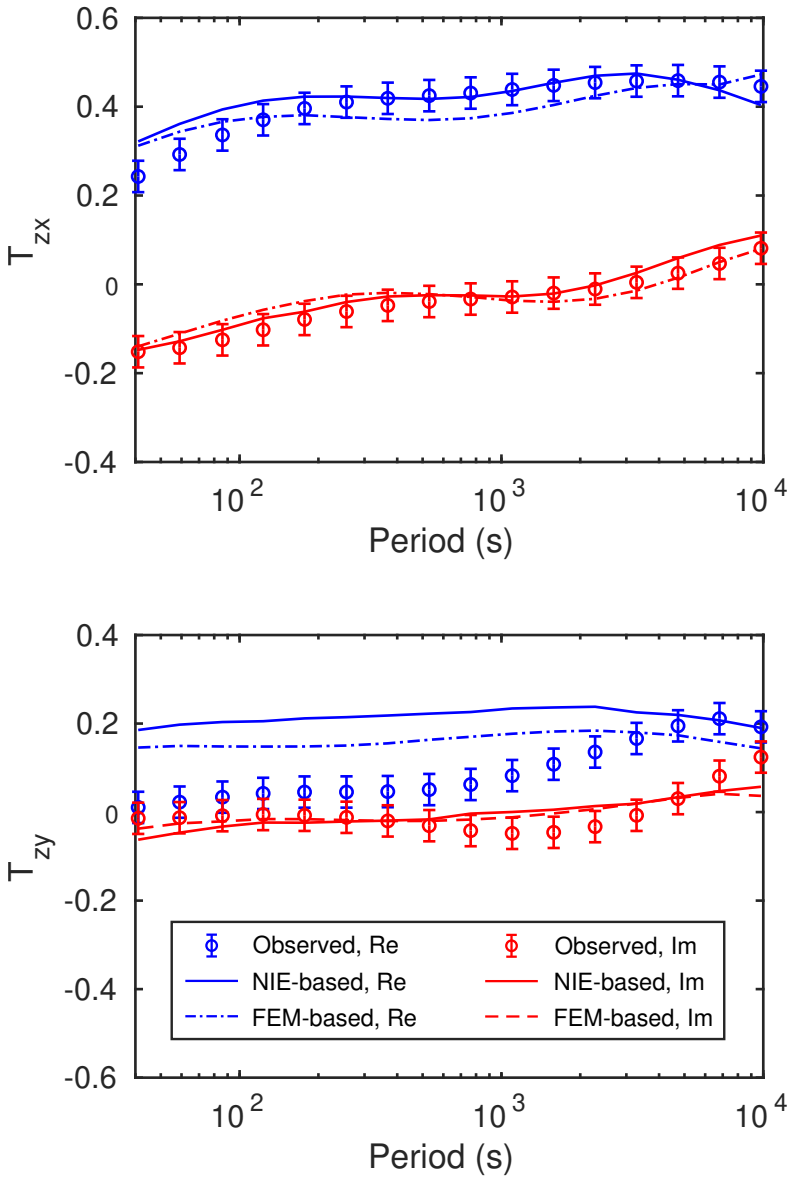

Figure 13. Modeled and observed tippers at the GAN observatory. The observed and FEM-based tippers are taken from (Morschhauser et al. 2019). Uncertainties of the observed responses are indicated by error bars.

resolution bathymetry data (The GEBCO_2014 Grid, www.gebco.net). We thank Achim Morschhauser for sharing with us the 1-D conductivity profile beneath GAN observatory, and the observed MT at GAN observatory. We also thank William Lowrie for improving the English language of the paper. We are grateful to Alexander Grayver for meaningful discussions in the course of our model experiments with the GAN model. CC was partly supported by a grant from the China Scholarship Council Foundation (201806370223). MK

was supported by RFBR, grant 20-05-00001. AK and CC were partially supported by the European Space Agency through the Swarm DISC project. The comments by the editor Ute Weckmann, Jochen Kamm and an anonymous reviewer greatly improved the manuscript.

REFERENCES

Avdeev, D., Kuvshinov, A., & Epova, K., 2002. Three-dimensional modeling of electromagnetic logs from inclined-horizontal wells, *Izv., Phys Solid Earth*, **38**, 975–980.

Avdeev, D., Kuvshinov, A., Pankratov, O., & Newman, G., 2002a. Three-dimensional induction logging problems, Part I: An integral equation solution and model comparisons, *Geophysics*, **67**(2), 413–426.

Avdeev, D. B., Kuvshinov, A. V., Pankratov, O. V., & Newman, G. A., 1997. High-performance three-dimensional electromagnetic modelling using modified Neumann series. Wide-band numerical solution and examples, *Journal of geomagnetism and geoelectricity*, **49**(11-12), 1519–1539.

Banks, R. J., 1969. Geomagnetic variations and the electrical conductivity of the upper mantle, *Geophysical Journal of the Royal Astronomical Society*, **17**(5), 457–487.

Becker, J., Sandwell, D., Smith, W., Braud, J., Binder, B., Depner, J., Fabre, D., Factor, J., Ingalls, S., Kim, S., et al., 2009. Global bathymetry and elevation data at 30 arc seconds resolution: Srtm30_plus, *Marine Geodesy*, **32**(4), 355–371.

Bohlander, J. & Scambos, T., 2007. Antarctic coastlines and grounding line derived from MODIS Mosaic of Antarctica (MOA), *National Snow and Ice Data Center, Boulder, CO, USA*.

Canning, F. X., 1989. Singular value decomposition of integral equations of EM and applications to the cavity resonance problem, *IEEE transactions on antennas and propagation*, **37**(9), 1156–1163.

Chave, A. D. & Jones, A. G., 2012. *The magnetotelluric method: Theory and practice*, Cambridge University Press.

Chen, C., Kruglyakov, M., & Kuvshinov, A., 2020. A new method for accurate and efficient modeling of the local ocean induction effects. Application to long-period responses from island geomagnetic observatories, *Geophysical Research Letters*, **47**(8), e2019GL086351.

Chopping, R. G., Duan, J., Czarnota, K., & Kemp, T., 2016. AusLAMP long period magnetotellurics: progress update and new insights into Victorian geology and mineral prospectivity, *AGUFM*, **2016**, GP41A–03.

Dong, H. & Egbert, G. D., 2019. Divergence-free solutions to electromagnetic forward and adjoint problems: a regularization approach, *Geophysical Journal International*, **216**(2), 906–918.

Dong, S. & Li, T., 2010. SinoProbe - A multidisciplinary research program of Earth sciences in China, *AGU Fall Meeting Abstracts*, pp. T42B–08.

Egbert, G. D. & Kelbert, A., 2012. Computational recipes for electromagnetic inverse problems, *Geophysical Journal International*, **189**(1), 251–267.

Farquharson, C. G. & Miensopust, M. P., 2011. Three-dimensional finite-element modelling of magnetotelluric data with a divergence correction, *Journal of Applied Geophysics*, **75**(4), 699–710.

Grayver, A. V. & Bürg, M., 2014. Robust and scalable 3-D geo-electromagnetic modelling approach using the finite element method, *Geophysical Journal International*, **198**(1), 110–125.

Grayver, A. V. & Kolev, T. V., 2015. Large-scale 3D geoelectromagnetic modeling using parallel adaptive high-order finite element method, *Geophysics*, **80**(6), E277–E291.

Grayver, A. V., Schnepf, N. R., Kuvshinov, A. V., Sabaka, T. J., Manoj, C., & Olsen, N., 2016. Satellite tidal magnetic signals constrain oceanic lithosphere-asthenosphere boundary, *Science advances*, **2**(9), e1600798.

Gumerov, N. A. & Duraiswami, R., 2005. *Fast multipole methods for the Helmholtz equation in three dimensions*, Elsevier.

Haber, E. & Ascher, U. M., 2001. Fast finite volume simulation of 3D electromagnetic problems with highly discontinuous coefficients, *SIAM Journal on Scientific Computing*, **22**(6), 1943–1961.

Haber, E. & Ruthotto, L., 2014. A multiscale finite volume method for Maxwell's equations at low frequencies, *Geophysical Journal International*, **199**(2), 1268–1277.

Han, B., Li, Y., & Li, G., 2018. 3D forward modeling of magnetotelluric fields in general anisotropic media and its numerical implementation in Julia, *Geophysics*, **83**(4), F29–F40.

Hursan, G. & Zhdanov, M. S., 2002. Contraction integral equation method in three-dimensional electromagnetic modeling, *Radio Science*, **37**(6), 1–13.

Jahandari, H. & Farquharson, C. G., 2014. A finite-volume solution to the geophysical electromagnetic forward problem using unstructured grids, *Geophysics*, **79**(6), E287–E302.

Johansen, S. E., Panzner, M., Mittet, R., Amundsen, H. E. F., Lim, A., Vik, E., Landrø, M., & Arntsen, B., 2019. Deep electrical imaging of the ultraslow-spreading Mohns Ridge, *Nature*, **567**(7748), 379–383.

Kamm, J. & Pedersen, L. B., 2014. Inversion of airborne tensor VLF data using integral equations, *Geophysical Journal International*, **198**(2), 775–794.

Karato, S.-i. & Wang, D., 2013. Electrical conductivity of minerals and rocks, *Physics and Chemistry of the Deep Earth*, pp. 145–182.

Key, K. & Weiss, C., 2006. Adaptive finite-element modeling using unstructured grids: The 2D magnetotelluric example, *Geophysics*, **71**(6), G291–G299.

Khan, A., 2016. On earth's mantle constitution and structure from joint analysis of geophysical and laboratory-based data: An example, *Surveys in Geophysics*, **37**(1), 149–189.

Koyama, T., Utada, H., & Avdeev, D., 2008. Fast and memory-saved 3-D forward modeling code for MT by using integral equation method, in *Abstract Book, Proceedings of the 19th Workshop on Electromagnetic induction in the Earth*.

Kruglyakov, M. & Bloshanskaya, L., 2017. High-performance parallel solver for integral equations of electromagnetics based on galerkin method, *Mathematical Geosciences*, **49**(6), 751–776.

Kruglyakov, M. & Kuvshinov, A., 2018. Using high-order polynomial basis in 3-D EM forward modeling based on volume integral equation method, *Geophysical Journal International*, **213**(2), 1387–1401.

Kuvshinov, A., 2008. 3-D global induction in the oceans and solid Earth: recent progress in modeling magnetic and electric fields from sources of magnetospheric, ionospheric and oceanic origin, *Surveys in Geophysics*, **29**(2), 139–186.

Kuvshinov, A., Utada, H., Avdeev, D., & Koyama, T., 2005. 3-D modelling and analysis of Dst C-responses in the North Pacific Ocean region, revisited, *Geophysical Journal International*, **160**(2), 505–526.

Li, G., Cai, H., & Li, C.-F., 2019a. Alternating joint inversion of controlled-source electromagnetic and seismic data using the joint total variation constraint, *IEEE Transactions on Geoscience and Remote Sensing*, **57**(8), 5914–5922.

Li, J., Liu, J., Egbert, G. D., Liu, R., Guo, R., & Pan, K., 2019b. An efficient preconditioner for 3-D finite difference modeling of the electromagnetic diffusion process in the frequency domain, *IEEE Transactions on Geoscience and Remote Sensing*, **58**(1), 500–509.

Mackie, R. L., Smith, J. T., & Madden, T. R., 1994. Three-dimensional electromagnetic modeling using finite difference equations: The magnetotelluric example, *Radio Science*, **29**(4), 923–935.

Mitsuhata, Y. & Uchida, T., 2004. 3D magnetotelluric modeling using the T-Ω finite-element method, *Geophysics*, **69**(1), 108–119.

Morschhauser, A., Grayver, A., Kuvshinov, A., Samrock, F., & Matzka, J., 2019. Tippers at island geomagnetic observatories constrain electrical conductivity of oceanic lithosphere and upper mantle, *Earth, Planets and Space*, **71**(1), 1–9.

Newman, G. A. & Alumbaugh, D. L., 2002. Three-dimensional induction logging problems, Part 2: A finite-difference solution, *Geophysics*, **67**(2), 484–491.

Nie, X. C., Yuan, N., & Liu, R., 2013. A fast integral equation solver for 3D induction well logging in formations with large conductivity contrasts, *Geophysical Prospecting*, **61**(3), 645–657.

Olsen, N. & Floberghagen, R., 2018. Exploring Geospace from Space: the Swarm Satellite Constellation Mission, *Space Research Today*, **203**, 61–71.

Pankratov, O. & Kuvshinov, A., 2016. Applied mathematics in EM studies with special emphasis on an uncertainty quantification and 3-D integral equation modelling, *Surveys in Geophysics*, **37**(1), 109–147.

Phillips, J. R. & White, J. K., 1997. A precorrected-FFT method for electrostatic analysis of complicated 3-D structures, *IEEE Transactions on Computer-Aided Design of Integrated Circuits and Systems*, **16**(10), 1059–1072.

Ren, Z., Kalscheuer, T., Greenhalgh, S., & Maurer, H., 2013a. A goal-oriented adaptive finite-element approach for plane wave 3-D electromagnetic modelling, *Geophysical Journal International*, **194**(2), 700–718.

Ren, Z., Kalscheuer, T., Greenhalgh, S., & Maurer, H., 2013b. Boundary element solutions for broad-band 3-D geo-electromagnetic problems accelerated by an adaptive multilevel fast multipole method, *Geophysical Journal International*, **192**(2), 473–499.

Ren, Z., Kalscheuer, T., Greenhalgh, S., & Maurer, H., 2014. A finite-element-based domain-decomposition approach for plane wave 3D electromagnetic modeling, *Geophysics*, **79**(6), E255–E268.

Schultz, A., 2010. EMScope: A Continental Scale Magnetotelluric Observatory and Data Discovery Resource, *Data Science Journal*, **8**(February), IGY6–IGY20.

Singer, B. S., 2008. Electromagnetic integral equation approach based on contraction operator and solution optimization in Krylov subspace, *Geophysical Journal International*, **175**(3), 857–884.

Snyder, J., 1982. Map projections used by the US Geological survey, Tech. rep., US Government Printing Office.

St-Louis, B., Sauter, E., & Coles, R., 2011. INTERMAGNET technical reference manual, version 4.5, INTERMAGNET.

Sun, J. & Kuvshinov, A., 2015. Accelerating EM integral equation forward solver for global geomagnetic induction using SVD based matrix compression method, *Geophysical Journal International*, **200**(2), 1005–1011.

Wessel, P. & Smith, W. H., 1996. A global, self-consistent, hierarchical, high-resolution shoreline database, *Journal of Geophysical Research: Solid Earth*, **101**(B4), 8741–8743.

Yoshino, T., 2010. Laboratory electrical conductivity measurement of mantle minerals, *Surveys in Geophysics*, **31**(2), 163–206.

Zhdanov, M. S., Varentsov, I. M., Weaver, J. T., Golubev, N. G., & Krylov, V. A., 1997. Methods for modelling electromagnetic fields results from COMMEMI - The international project on the comparison of modelling methods for electromagnetic induction, *Journal of Applied Geophysics*, **37**(3-4), 133–271.

APPENDIX A: BASIS FUNCTIONS CONSTRUCTION

Let domain $\widetilde{\mathrm{V}}$ be divided into $N^{\mathrm{cells}} = N_x N_y N_z$ rectangular cells

$$\widetilde{\mathrm{V}}_n = [x_n \; x_n + h_x^n] \times [y_n \; y_n + h_y^n] \times [z_n \; z_n + h_z^n], \quad n = 1, 2, \ldots, N^{\mathrm{cells}}. \tag{A.1}$$

Then, the local scalar basis functions $\Psi_n^{n_x,n_y,n_z}(x,y,z)$ for each cell $\widetilde{\mathrm{V}}_n$ are expressed as

$$\Psi_n^{n_x,n_y,n_z}(x,y,z) = \frac{2\sqrt{2}}{\sqrt{h_x^n h_y^n h_z^n}} L_{n_x}\left(2\frac{x-x_n}{h_x^n} - 1\right) \times L_{n_y}\left(2\frac{y-y_n}{h_y^n} - 1\right) \times L_{n_z}\left(2\frac{z-z_n}{h_z^n} - 1\right). \tag{A.2}$$

Here, $L_n = \sqrt{\frac{2n+1}{2}} P_n$, P_n is the Legendre polynomial of n-th order, and $n_{x(y,z)} = 0, 1, \ldots, N^P_{x(y,z)}$, where $N^P_{x(y,z)}$ are the maximum polynomial orders along x-, y- and z-directions.

Then, the vector basis functions $\mathbf{\Psi}_n$, $n = 1, 2, \ldots, N$, $N = 3N^{\mathrm{cells}} \left(N_x^P + 1\right)\left(N_y^P + 1\right)\left(N_z^P + 1\right)$ are assembled as $\mathbf{\Psi} = (\Psi_x, \Psi_y, \Psi_z)$, where $\Psi_{x,y,z}$ stand for $\Psi_n^{n_x,n_y,n_z}$ in eq. (A.2). Note that $\mathbf{\Psi}_n$ are orthonormal at $\widetilde{\mathrm{V}}_n$ due to the orthonormality of the L_n. To obtain the orthonormality of $\mathbf{\Psi}_n$ at the whole domain $\widetilde{\mathrm{V}}$ one just needs to define $\mathbf{\Psi}_n(\mathbf{r}) = 0, \mathbf{r} \notin \widetilde{\mathrm{V}}_n$.

APPENDIX B: CALCULATING INTEGRALS OF THE BASIS FUNCTIONS PRODUCTS

As explained in the main text, the realization of the nested approach requires computation of the following expression

$$\left(\mathbf{E}^{add\,(c)}, \mathbf{\Psi}_{n,k}^{(f),\,\mathrm{loc}}\right) \approx \sum_{\mathrm{V}_m^{(c)} \subset \mathrm{V}^{\mathrm{loc}}} \sum_{l=1}^{K_c} u_{m,l}^{add\,(c)} \int\limits_{\mathrm{V}_n^{(f),\mathrm{loc}}} \mathbf{\Psi}_{n,k}^{(f),\,\mathrm{loc}}(\mathbf{r}) \mathbf{\Psi}_{m,l}^{(c)}(\mathbf{r}) d\mathrm{V}_n^{(f),\mathrm{loc}}, \tag{B.1}$$
$$n = 1, 2, \ldots, N_f, \quad k = 1, 2, \ldots, K_f.$$

or, in other words, one has to calculate the integral over $\mathrm{V}_n^{(f),\mathrm{loc}}$ in eq. (B.1). Below we show how this integral can be calculated analytically.

To do this, let us first substitute the basis functions introduced in Appendix A into the integral in eq. (B.1). As a result we have

$$\int\limits_{\mathrm{V}_m^{(f),\mathrm{loc}}} \Psi_m^{(f),\mathrm{loc}}(\mathbf{r})\Psi_n^{(c)}(\mathbf{r})d\mathrm{V}_m^{(f),\mathrm{loc}} = \sqrt{\frac{2n_x^{(c)}+1}{h_x^{n(c)}}\frac{2n_y^{(c)}+1}{h_y^{n(c)}}\frac{2n_z^{(c)}+1}{h_z^{n(c)}}\frac{2n_x^{(f)}+1}{h_x^{m(f)}}\frac{2n_y^{(f)}+1}{h_y^{m(f)}}\frac{2n_z^{(f)}+1}{h_z^{n(f)}}}$$
$$\times \int\limits_{x_m^{(f)}}^{x_m^{(f)}+h_x^{m(f)}} P_{n_x}^{(c)}\left(2\frac{x-x_n^{(c)}}{h_x^{n(c)}}-1\right) P_{n_x}^{(f),\mathrm{loc}}\left(2\frac{x-x_m^{(f)}}{h_x^{m(f)}}-1\right) dx$$
$$\times \int\limits_{y_m^{(f)}}^{y_m^{(f)}+h_y^{m(f)}} P_{n_y}^{(c)}\left(2\frac{y-y_n^{(c)}}{h_y^{n(c)}}-1\right) P_{n_y}^{(f),\mathrm{loc}}\left(2\frac{y-y_m^{(f)}}{h_y^{m(f)}}-1\right) dy$$
$$\times \int\limits_{z_m^{(f)}}^{z_m^{(f)}+h_z^{m(f)}} P_{n_z}^{(c)}\left(2\frac{z-z_n^{(c)}}{h_z^{n(c)}}-1\right) P_{n_z}^{(f),\mathrm{loc}}\left(2\frac{z-z_m^{(f)}}{h_z^{m(f)}}-1\right) dz. \tag{B.2}$$

As is seen from eq. (B.2) it is sufficient to show how to compute one, for instance, the first integral; other integrals can be computed in a similar way. Let us introduce the following notations

$$s=x,\ s_1=x_m^{(f)},\ s_2=x_m^{(f)}+h_x^{m(f)},\ q_1=x_n^{(c)},\ q_2=x_n^{(c)}+h_x^{m(c)},\ l=n_x^{(c)},\ k=n_x^{(f)}. \tag{B.3}$$

Then the first integral in eq. (B.2), with the corresponding prefactor, is rewritten as

$$\begin{aligned}
&\frac{2n_x^{(f)}+1}{h_x^{m(f)}} \int\limits_{x_m^{(f)}}^{x_m^{(f)}+h_x^{m(f)}} P_{n_x}^{(c)}\left(2\frac{x-x_n^{(c)}}{h_x^{n(c)}}-1\right) P_{n_x}^{(f),\mathrm{loc}}\left(2\frac{x-x_{m1}^{(f)}}{h_x^{m(f)}}-1\right) dx \\
&= \frac{2k+1}{s_2-s_1}\int\limits_{s_1}^{s_2} P_l\left(2\frac{s-q_1}{q_2-q_1}-1\right) P_k\left(2\frac{s-s_1}{s_2-s_1}-1\right) ds \\
&= \frac{2k+1}{t_2-t_1}\int\limits_{t_1}^{t_2} P_l(t)P_k\left(2\frac{t-t_1}{t_2-t_1}-1\right) dt \\
&= C_l^k(t_1,t_2),
\end{aligned} \tag{B.4}$$

where

$$t_1 = 2\frac{s_1 - \frac{q_2+q_1}{2}}{q_2 - q_1}, \quad t_2 = 2\frac{s_2 - \frac{q_2+q_1}{2}}{q_2 - q_1}. \tag{B.5}$$

Let us further introduce an auxiliary integral

$$\dot{C}_l^k(t_1, t_2) = \frac{2k+1}{t_2 - t_1}\frac{1}{l}\int_{t_1}^{t_2} \dot{P}_l(t) P_k\left(2\frac{t - t_1}{t_2 - t_1} - 1\right) dt, \tag{B.6}$$

where $\dot{P}_l(t) = \frac{d}{dt}P_l(t)$. Finally, using recursion formulas for Legendre's polynomials and their derivatives, after some algebra we obtain a set of recursion formulas that allows us to calculate $C_l^k(t_1, t_2)$, i.e., the required integral

$$\begin{aligned}
C_l^k(t_1, t_2) &= \frac{1}{1 + \frac{k+1}{l}}\left(\frac{t_2 - t_1}{2}\frac{2k+1}{2k-1}\dot{C}_l^{k-1}(t_1, t_2) + \frac{t_2 + t_1}{2}\dot{C}_l^k(t_1, t_2) - \left(1 - \frac{1}{l}\right)\dot{C}_{l-1}^k(t_1, t_2)\right), \\
\dot{C}_l^k(t_1, t_2) &= \left(2 - \frac{1}{l}\right)C_{l-1}^k(t_1, t_2) + \left(1 - \frac{2}{l}\right)\dot{C}_{l-2}^k(t_1, t_2), \\
C_l^0(t_1, t_2) &= \left.\frac{P_{l+1}(t) - P_{l-1}(t)}{(2l+1)(t_2 - t_1)}\right|_{t=t_1}^{t=t_2}, \\
\dot{C}_l^0(t_1, t_2) &= \frac{1}{l}\frac{P_l(t_2) - P_l(t_1)}{t_2 - t_1}, \\
C_k^k(t_1, t_2) &= \left(\frac{t_2 - t_1}{2}\right)^k, \\
C_l^k(t_1, t_2) &= 0, l < k, \\
\dot{C}_l^k(t_1, t_2) &= 0, l \leq k.
\end{aligned} \tag{B.7}$$